

# Three Dimensional Simulations of Vertical Magnetic Flux in the Immediate Vicinity of Black Holes

Brian Punsly<sup>1</sup>, Igor V. Igumenshchev<sup>2</sup>, Shigenobu Hirose<sup>3</sup>

brian.punsly@verizon.net

## ABSTRACT

This article reports on three-dimensional (3-D) MHD simulations of non-rotating and rapidly rotating black holes and the adjacent black hole accretion disk magnetospheres. A particular emphasis is placed on the vertical magnetic flux that is advected inward from large radii and threads the equatorial plane near the event horizon. In both cases of non-rotating and rotating black holes, the existence of a significant vertical magnetic field in this region is like a switch that creates powerful jets. There are many similarities in the vertical flux dynamics in these two cases in spite of the tremendous enhancement of azimuthal twisting of the field lines and enhancement of the jet power because of an “ergospheric disk” in the Kerr metric. A 3-D approach is essential because two-dimensional axisymmetric flows are incapable of revealing the nature of vertical flux near a black hole. Poloidal field lines from the ergospheric accretion region have been visualized in 3-D and much of the article is devoted to a formal classification of the different manifestations of vertical flux in the Kerr case.

*Subject headings:* Black hole physics - magnetohydrodynamics -galaxies: jets—galaxies: active — accretion disks

## 1. Introduction

It is widely believed that magnetized plasma ejected from the vicinity of a supermassive black hole is the origin of the relativistic jets that have been detected in extragalactic radio

---

<sup>1</sup>4014 Emerald Street No.116, Torrance CA, USA 90503 and International Center for Relativistic Astrophysics, ICRANet, Piazza della Repubblica 10 Pescara 65100, Italy

<sup>2</sup>Laboratory for Laser Energetics, University of Rochester  
250 East River Road, Rochester, NY 14623

<sup>3</sup>The Earth Simulator Center, JAMSTEC 3173-25 Showamachi, Kanazawa-ku, Yokohama, Kanagawa 236-0001, Japan

sources. Furthermore, such jets are believed to be highly magnetized at their launch point in order for jet plasma to achieve highly relativistic velocities. One of the biggest controversies in the theory of relativistic, extragalactic jets is whether they initiate from local turbulent magnetic fields created in an accretion flow or from a large scale reservoir of poloidal flux that is advected inward from large distances. The implication of the first scenario is that the coherent field within the dense gas is inhibited by the turbulent magnetic diffusivity of the plasma (van Ballegoijen 1989; Lubow et al 1994). As a corollary to this, it customarily concluded that the accretion disk cannot maintain a strong magnetosphere and therefore the jet power would be quite small relative to FRII (Fanaroff-Riley type II) radio sources (Ghosh and Abramowicz 1997).<sup>1</sup> The only place in which a strong field can exist in this scenario is pinned against the event horizon, in the vortex of the accretion flow, and then only under a select set of circumstances (Beckwith et al 2008). Conversely, the second scenario implies that large scale poloidal magnetic fields can be maintained by the accreting gas all the way down to the black hole (Bisnovatyi-Kogan and Ruzmaikin 1974, 1976; Narayan et al 2003). Provided that the turbulence in the accretion flow does not induce an outward diffusion of magnetic flux that is too rapid, the inner regions of the accretion disk will support significant vertical flux (Rothstein and Lovelace 2008). In the weak field limit, modest mildly relativistic jets can be driven by magneto-centrifugal forces (Blandford and Payne 1982). If a strong vertical field is accumulated in the inner regions of the disk, a relativistic Poynting jet forms that is far more powerful than its magneto-centrifugal counterpart (Lovelace 1976; Blandford 1976; Ustyugova et al 2000). If the vertical flux is accumulated within the plunge region, an ergospheric disk and the associated Poynting jet can form (Punsly and Coroniti 1990; Punsly 2008). This is of particular interest to the study of powerful jets in radio loud AGN since the jet power is increased an order of magnitude over the Poynting jets from flux that is merely pinned to the event horizon of a rapidly rotating black hole.

The longstanding controversy over the existence of significant vertical flux in black hole accretion disks is rooted in a legacy of theoretical studies. The time evolution of vertical flux depends on critical assumptions about the accreting gas that are not well understood in a quasar environment (Meier 2004; Spruit and Uzdensky 2005; Shibata et al 1990; Kato et al 2004; Rothstein and Lovelace 2008). Numerical methods have the tremendous advantage of being able to depict the very nonlinear magnetic flux evolution of scenarios based on said assumptions - something that can only be addressed with crude approximations theoretically. Given that the potential existence of vertical flux in the equatorial accretion flow is fundamental to the theory of black hole driven jets, we use the data from long term 3-D simulations, that contain significant vertical flux near the black hole, in order to shed light

---

<sup>1</sup>these arguments have been challenged by Reynolds et al (2006)

on the general properties of these flux distributions. This paper is not an overview of the set of numerical assumptions, initial conditions and black hole states that give rise to such features. This is far beyond the state of this burgeoning field of numerical work. Instead it reports on the first two known anecdotal cases of long term 3-D simulations that show significant magnetic flux adjacent to the black hole. As a pioneering work in this area, it is by no means complete. Our particular emphasis is on exploring the possible varieties of self-consistent MHD structures that can support significant vertical flux near black holes. For our purposes, these simulations offer a wealth of information and revelations.

This paper employs both 2-D and 3-D numerical simulations to investigate the nature of vertical flux near black holes. We explore two extreme versions of a black hole. First, a non-rotating black hole in the Pseudo-Newtonian approximation with a continuous net magnetic flux accretion (section 3). Additionally, we look at a near maximally rotating black hole ( $a/M = 0.99$ , where "a" is the angular momentum per unit mass, "M", of the black hole in geometrized units) with zero net flux in the initial state and no flux accretion from the outer boundary afterwards (section 4). Comparing and contrasting these simulations in section 5 offers new insights into the nature of vertical flux near black holes.

Perfect magnetohydrodynamic (simply MHD hereafter) numerical simulations offer us a virtual laboratory for exploring the possible self-consistent MHD structures that might exist near black holes. We consider this tool only as such and we do not offer them any more import than this. Thus, it is necessary to stress that we do not claim

1. that the simulations that are used to determine these results are representative of actual AGN central engines, nor
2. that the results that we see in the simulation are independent of the initial conditions and the assumptions of the numerical code, nor
3. that the perfect MHD assumption implemented in the numerical code is applicable to the extremely hot and very turbulent plasma in the inner accretion flow. In particular, the manner in which flux diffuses and reconnects, nor
4. that the results of these simulations are not influenced by numerical diffusion.

A second goal of this study is to consider visualization techniques for studying complicated magnetospheric phenomena. For example, it has been discovered that the base of the solar magnetosphere is filled with powerful, complicated geometrical structures such as bundles of field lines that form bent semi-circular arcs in which the individual lines twist around each other. As with the sun, the complexity of the 3-D structures can not be readily understood with 2-D visualization techniques (Dorch et al 1999; Archontis and Hood 2008; Warren

et al 2008). We anticipate that the inner parts of an accretion flow forming a quasar should have a magnetosphere with similar or greater complexity since it is extremely turbulent and hotter than the solar chromosphere (there is also strong azimuthal shearing due to the differentially rotating accretion flow that is far more severe than in the solar atmosphere). We have developed certain graphical techniques within a 3-D visualization platform, Paraview 3.3.0. We show that there is a tremendous distinction between azimuthally averaged plots and the 3-D visualization. The actual field line geometry is virtually impossible to figure out from the 2-D averages because the magnetosphere is very inhomogeneous and twisted. We found it necessary to use 3-D animations of a camera revolving around the black hole in order to get a truly clear picture since there are so many distortions from perspective and there are always lines of sight that are blocked by other field lines, obscuring gas or the black hole itself. In section 4, we use our 3-D visualization techniques to describe four distinct vertical field line varieties that arise in simulations of the innermost accretion flow near a rapidly rotating black hole.

## 2. A Fundamental Topological Issue

In this section, we comment on how different initial conditions and boundary conditions can suppress or enhance, the amount of vertical flux near a black hole. We believe that the presence of vertical flux in the inner accretion flow is rendered to a basic topological consideration that we motivate in this discussion and figure 1.

The simulations in Igumenshchev (2008) considered a net vertical flux that accretes towards a black hole in both 2-D and 3-D from the outer regions of the simulation. Unlike the simulations in De Villiers and Hawley (2003a); De Villiers et al (2003b); Hirose et al (2004); Krolik et al (2005); Hawley and Krolik (2006); Beckwith et al (2008) and McKinney and Gammie (2004); McKinney (2005) that considered a finite toroidal pool of gas, threaded by poloidal loops of like orientation, Igumenshchev (2008) considered an endless supply of gas from the outer boundary. This is a major fundamental distinction from the poloidal loop simulations. In the poloidal loop simulations, a finite amount of flux reaches the accretion vortex. The vortex or funnel fills with the leading edges of the loops of like orientation. The magnetosphere in the vortex is then only modestly perturbed by additional vertical flux of random orientation created by the MRI dynamo within the turbulent accretion flow (Beckwith et al 2008). By contrast, in the simulation presented in Igumenshchev (2008), a continuous supply of vertical flux approaches the accretion vortex all of the same orientation, even after the vortex is completely saturated with flux. The question is what does the numerical system do with the continual pile up of excess flux near the vortex in a frozen-in

accreting plasma? In the 2-D simulations of Igumenshchev (2008), a time-dependent behavior of the flow with two different field line topologies resulted near the black hole as shown in figure 1 (we describe these simulations in more detail in section 3).

Another line of 2-D research was initiated in Komissarov (2004). He explored the  $l=1$ ,  $m=0$ , vacuum field solution of Maxwell’s equations on a black hole background (known as the Wald solution) after it was filled with a diffuse plasma. The outer boundary condition was Bondi accretion. This problem is relevant because the initial state has vertical flux through the equatorial plane just outside the event horizon. It was found that initially the accreting low density plasma accumulated in an arrested state in the equatorial plane. However, eventually, as the arrested gas continued to accumulate, it achieved enough inertia to drag the vertical field radially inward in the equatorial plane into the event horizon making an ”hourglass” topology (similar to figure 1b). There was no vertical flux through the equatorial plane, near the black hole. This was a similar topology to what was observed generally in the thick tori accretion models of De Villiers and Hawley (2003a); De Villiers et al (2003b); Hirose et al (2004); Krolik et al (2005); Beckwith et al (2008) and McKinney and Gammie (2004); McKinney (2005). This led Komissarov and McKinney (2007) to consider this as a general topology for black hole magnetospheres - approximately radial flux at the horizon and none through the equatorial plane near the event horizon.

In many respects, the works of Igumenshchev (2008) and Komissarov (2004); Komissarov and McKinney (2007) have crystalized the discussion of vertical flux near black holes into a simple topological dichotomy: is the astrophysical state an ”hourglass” topology (right frame of figure 1, figure 1b) or a magnetically arrested topology (the left frame of figure 1, figure 1a)? There is numerical support for both the hourglass and the vertical topology within the literature. This article is not one to proclaim which numerical simulation is the ”one” that represents nature. This could not be demonstrated with anything that has been done numerically or is known theoretically about the physical state of accreting quasar plasma. All we can say is that simple approximations to the actual physical system were evolved with some numerical codes and this is what occurred.

### 3. Long Term Flux Accretion in the Pseudo-Newtonian Potential

In this section, we consider the data from the previously published simulations in Igumenshchev (2008) to lay the groundwork for demonstrating the close similarity between the types of accretion flows found in Igumenshchev (2008) and in fully relativistic simulation KDJ that is described in section 4. For the purposes of this paper, we reanalyze the data to explicitly show the vertical magnetic field evolution in the 3-D simulations. Previously, only

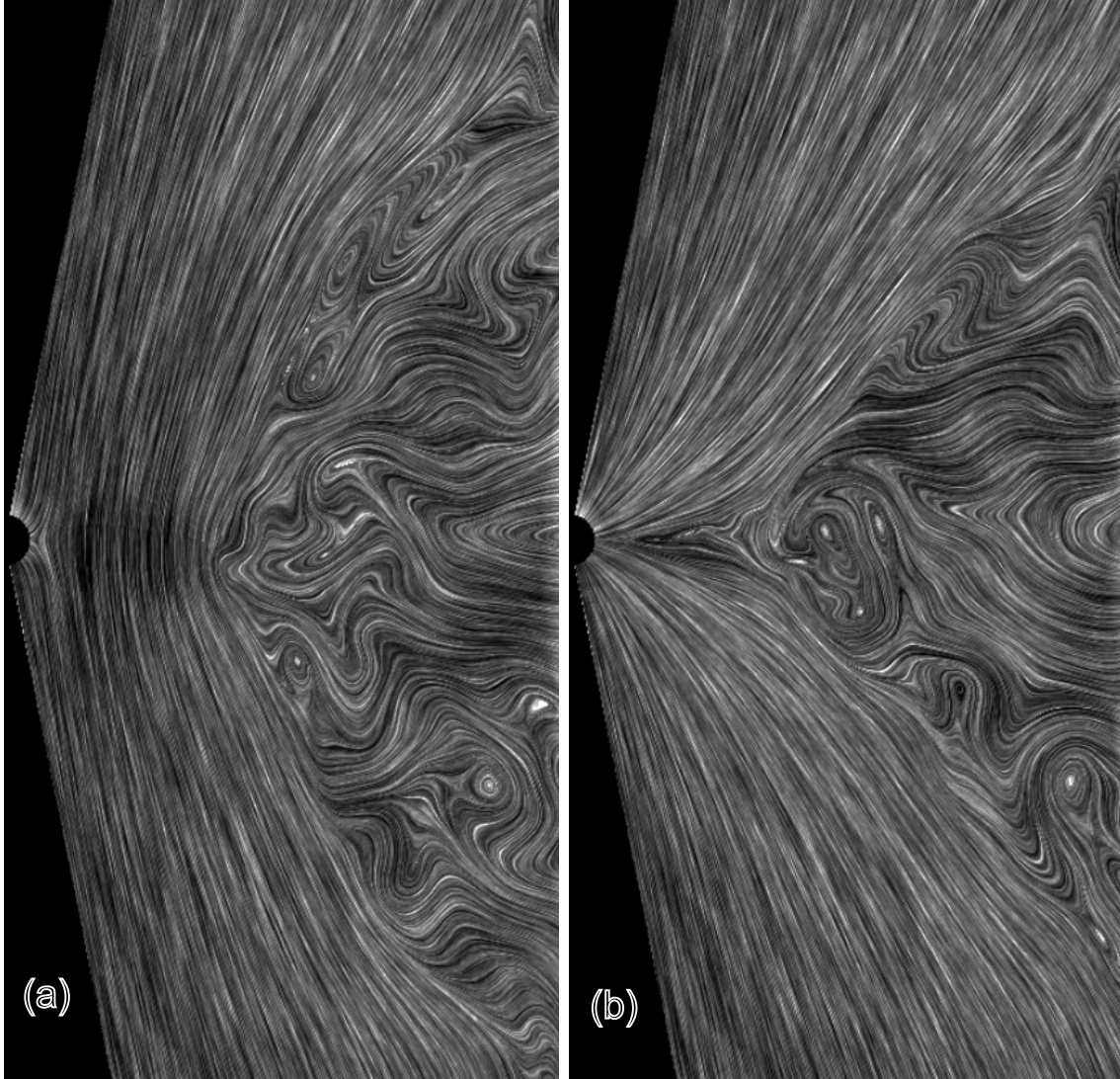


Fig. 1.— The poloidal magnetic field in the 2-D simulation of Igumenshchev (2008). The figure is a magnification of the inner region of figures 2a and 2b from Igumenshchev (2008). The topology of the right frame, figure 1b, is the "hourglass" shape that has very little vertical flux penetrating the equatorial plane near the event horizon. The gas is free to plunge into the black hole radially. The left frame, figure 1a, represents the magnetically arrested accretion state in which the preponderance of flux near the black hole penetrates the equatorial plane.

plots pertaining to the density evolution were published. We also explicitly demonstrate the connection between the evolution of strongly magnetized islands and density variations within the 3-D flows near the black hole. A connection was mentioned in Igumenshchev (2008), but never shown in detail. These are crucial details that we will need to make a comparison and contrast to an independent 3-D numerical simulation that we analyze in section 4. The fact that similar magnetic islands exist in two different simulations enhances the robustness of our analysis.

The simulations in Igumenshchev (2008) expanded on the work of Igumenshchev et al (2003) by studying radiatively inefficient accretion disks with poloidal magnetic fields in more detail. These works simulated accretion flows around a Schwarzschild black hole using the equations of non-relativistic ideal MHD (Landau and Lifshitz (1987)), in which the black hole gravity is approximated using a pseudo-Newtonian potential (Paczynski and Wiita (1980)). A major difference between the numerical methods of Igumenshchev et al (2003); Igumenshchev (2008) and the simulations that were presented in De Villiers and Hawley (2003a); De Villiers et al (2003b); Hirose et al (2004); Krolik et al (2005); Hawley and Krolik (2006); Beckwith et al (2008) and McKinney and Gammie (2004); McKinney (2005) is that they allow for the astrophysical meaningful condition that material is continuously injected into the system from a distant injection surface,  $R_{inj}$ , as opposed to evolving a finite pool of material that was deposited in the initial state.

The simulations in Igumenshchev (2008) are started in 2D, assuming axial symmetry, with an injection of mass with the Keplerian angular momentum in a slender torus, which is located in the equatorial plane at  $R_{inj} = 210 R_g$ , just inside the outer calculational boundary  $R_{out} = 220 R_g$  (where  $R_g = 2GM/c^2$  is the gravitational radius of the black hole). Initially there is no magnetic flux and the injected mass forms a steady (non-accreting) thick torus. The MHD portion of the simulations are started at  $t = 0$  from this steady torus by initiating the injection of a poloidal magnetic field at  $R_{inj}$ . The method is the same as in Igumenshchev et al (2003). In each time step,  $i$ , field is introduced into the slender torus by adjusting the azimuthal component of the vector potential (all other components are set to zero) by  $A_\phi^i = A_\phi^{i-1} + \sqrt{8\pi(\Delta\rho)c_s^2/\beta_{inj}}\Delta$ , where  $(\Delta\rho)$  is the increase in density in the torus during the time step due to the injection of matter,  $c_s$  is the sound speed and  $\Delta$  is the grid spacing. The strength of the injected field can be limited by setting the minimum  $\beta_{inj}$ , which is the ratio of the gas pressure to the magnetic pressure at  $R_{inj}$ . Large scale magnetic stresses within the injected material allows for a redistribution of angular momentum. Thus, some of the injected matter loses angular momentum and accretes toward the black hole and some matter also flows out of the computational domain thereby removing excess angular momentum. The entire volume of the thick torus is filled by the field during about one orbital period,  $t_{orb}$ , estimated at  $R_{inj}$ . At this moment,  $t \simeq t_{orb}$ , the formation of accretion

flow begins as a result of redistribution of the angular momentum in the torus due to Maxwell stresses.

Various simulations of accreting vertical flux were run in Igumenshchev (2008) in which the only variable was  $\beta_{inj}$ , the relative strength of vertical magnetic field that was injected. It should be noted that in the absence of radiative losses the accretion flow structure is independent of the assumed mass accretion rate and the dependence on the black hole mass  $M$  come only through the spatial scales  $R \propto R_g$ . The basic trend was as follows, the smaller  $\beta_{inj}$  (the stronger the injected field) the weaker the MRI (turbulence) and the larger the magnetic stresses (i.e, the faster angular momentum is removed outward from the accretion flow and the more rapidly the plasma accretes toward the black hole). The simulation known as model B was investigated in the most detail in Igumenshchev (2008) and is defined by  $\beta_{inj} = 100$ . We will expand on the discussion of Igumenshchev (2008) in the context of the present topic in this section.

### 3.1. The 2-D Results

The initial evolution in the models in Igumenshchev (2008) was simulated in 2D. This allows one to consider longer evolution times in comparison to those that can be obtained in 3D simulations, because of the larger requirements for computational resources in the latter case. The 3D simulations are initiated from developed axisymmetric models. An extended duration 2-D run of model B was performed in parallel with the 3-D run. The relevant details are captured in figures 1a and 1b. The figure samples two data dumps, at  $t = 5.1153$  and  $t = 5.1458$  (left and right frames), given in units of the Keplerian orbital period at  $R_{inj} = 210R_g$ . The magnetic field lines are produced in figure 1, by the line integral convolution method (Cabral and Leedom 1993). The frame on the left (figure 1a) has a large patch of vertical flux through the equatorial plane that extends almost all the way to the inner circular calculational boundary,  $R_{in} = 2R_g$ . The field deviates from purely vertical near the equatorial plane extremely close to the boundary in order to meet the imposed boundary condition of no transverse magnetic field at the inner calculational boundary,  $R_{in}$ . Even with this boundary condition, the field is vertical at the equator for  $R - R_{in} > 0.75R_g$ . In this phase, the accretion flow is halted by the patch of strong vertical flux. This is the 2-D version of a magnetically arrested disk Igumenshchev et al (2003); Igumenshchev (2008).

The magnetically arrested portion displayed in figure 1a keeps accumulating mass and field as the accretion from large distances proceeds. However, the radial force balance between the trapped magnetic flux and the incoming gas is Rayleigh-Taylor unstable, but in 2-D there is the assumption of axisymmetry, so ingoing flutes of plasma can not slide by on



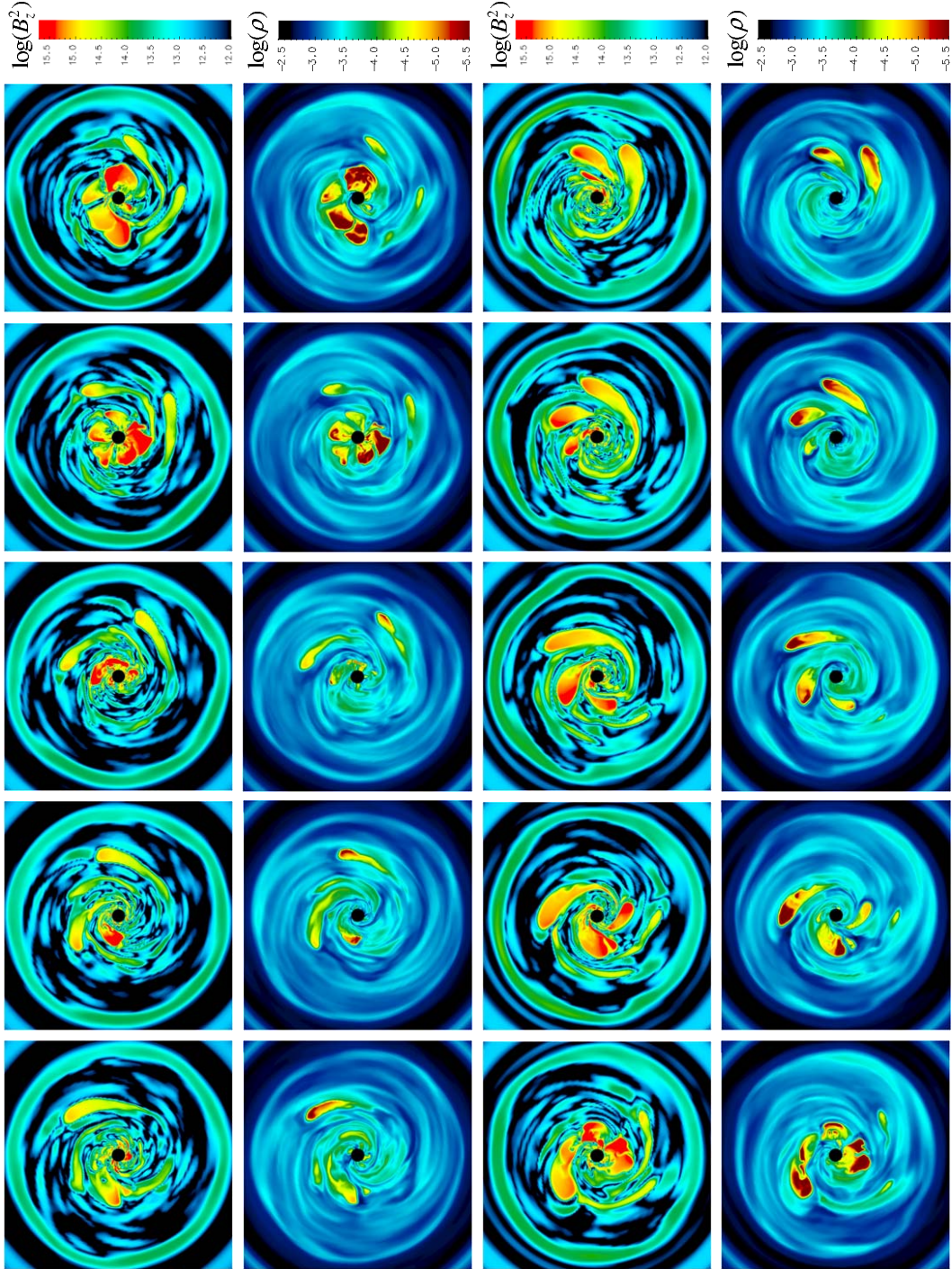


Fig. 2.— 10 consecutive time snapshots of the poloidal magnetic field and density in model B of Igumenshchev (2008). The left column and the second column are simultaneous consecutive time snapshots in the equatorial plane of  $B_z^2$  and density, respectively. Similarly for columns 3 and 4. The time increases from bottom to top and column 1 precedes column 3 (see text for details). The second and fourth columns are extracted from movie 1 that is on-line.

the side (the “side” is the the  $\phi$  direction) of islands of buoyant magnetic flux as it would in a 3-D Rayleigh Taylor interface. In 2-D, the mass density builds up until the increased attraction towards the gravitational center drags the field and ”stacked up” frozen-in plasma inward radially as in figure 1b. When the field attains this ”hour-glass” topology, the plasma is allowed to accrete freely into the black hole in the radial direction by just sliding along the field lines. Recall that the same situation occurred in the 2-D simulation of Komissarov (2004) that was discussed in the previous section.

The plasma drains down the ”hour-glass” rapidly. Once the density is sufficiently low, the field topology actually reverts back to the magnetically arrested topology of vertical flux near the inner boundary. A new magnetically arrested epoch is begun. Actually, the system spends almost all of its time in the magnetically arrested state as depicted in figure 1a and only goes into the the ”hour-glass” for brief instances separated by large time intervals. Compare this to the 2-D simulations of Komissarov and McKinney (2007), in which the field is in a pure hour-glass topology all of the time. In particular, figure 3 of Komissarov and McKinney (2007) shows an accretion disk flowing through the ”cusp” of the ”hour-glass” near the equatorial plane. By contrast, model-B of Igumenshchev (2008) is only rarely in this ”hour-glass” field topology and is in the magnetically arrested state the vast majority of the time. Recall, the fundamentally different assumptions made in these two articles. The Komissarov and McKinney (2007) accretion flow contains a finite amount of poloidal flux and there is no large reservoir of flux that accretes from large distances. By contrast, Igumenshchev (2008) assumes an eternal supply of gas and vertical field that can accrete from large distances.

### 3.2. The 3-D Results

Next we explore the more physically relevant 3-D portion of the simulations. Neither state in figure 1a nor figure 1b is achieved. In 2-D the two states in figure 1 are mutually exclusive in a temporal sense. In 3-D, the two states present in the 2-D flow seem to coexist simultaneously within the same flow. Not surprisingly, this leads to some nontrivial dynamics that we study by means of the series of snapshots presented in figure 2. Figure 2 represents 10 consecutive data dumps separated by  $\Delta t = 17.8M$ , where  $t$  is in geometrized units, and plots two quantities at each corresponding time, the logarithm of the density,  $\rho$  and the logarithm of the square of the vertical field,  $B_z^2$ , in the equatorial plane. Figure 2 contains a wealth of information that is far too detailed for a figure caption. From left to right, columns 1 and 3 are false color plots of  $\log(B_z^2)$ . Time progresses upward in each column and the column 1 precedes column 3. Columns 2 and 4 are false color contour plots of  $\log(\rho)$ .

These two columns are snapshots of the animation, movie 1, that is available in the on-line material. Note that the plasma rotates in the clockwise direction in figure 2.

The snapshots in figure 2 were chosen to elucidate the evolution of magnetic flux build-up in the inner regions of the accretion flow. Consider frame 1 in the first column. Blue represents a small vertical magnetic field component and red indicates a large vertical field component at the equator. There are actually small regions of strong vertical field just outside the inner calculational boundary. However, most of the vertical field is about an order of magnitude weaker in the remainder of the inner region. In frames 2 and 3 (from the bottom) in column 1, there is a definite accumulation of vertical flux near the inner boundary. The peak vertical flux close to the inner boundary is in frame 4. After this, the large patch of strong vertical field starts migrating away from the inner calculational boundary in frame 5.

Now consider the the second column. In this plot, the color scheme is reversed, blue is high density and red is low density. In the first three frames of column 2 (going from bottom to top) the density is high, in code units,  $\rho \sim 10^{-3} - 10^{-4}$  within the evolving magnetic islands. After the peak flux is accumulated near the inner calculational boundary in frame 4, the density drops precipitously,  $\rho \sim 10^{-5} - 10^{-5.5}$  within the magnetic islands. This is the equivalent to a local region of a magnetically arrested accretion flow. Very little mass penetrates the strong magnetic pressure barrier. In 2-D, this phenomena is global in figure 1a, but in 3-D it exists in localized regions with most of the plasma accreting along pathways the flow around the edges of these magnetic islands. In this context, we note that throughout the simulation, the vertical flux and density variations are not axisymmetric, but dominated by spiral modes with azimuthal wavenumbers,  $1 \leq m \lesssim 5$  (Igumenshchev 2008).

Regions of strong vertical flux ( $\beta \sim 0.01$ ) exist extremely close to the inner calculational boundary, much closer than in the 2-D case presented in figure 1a. The local magnetically arrested areas associated with the enhanced vertical field strength are inherently Rayleigh-Taylor unstable. The strong magnetic islands in frame 4 of column 1 begin to migrate slowly outward in frames 5 and 6 (the bottom frame of column 3). Furthermore, the large magnetic pressure in the magnetic islands makes them "over-pressurized" relative to regions outside the islands. The pressure begins to spread the islands apart in frame 5. Since the magnetic islands are low density they are weakly affected by gravity. By contrast, the dense accretion flow is strongly attracted to the central black hole. The magnetic islands therefore become buoyant within the dense accretion flow under the influence of the gravitational field. This makes them spiral outward in frames 6 - 9, creating a strong shear relative to the enveloping accretion flow. As the buoyant flux tubes spiral outward, magnetic flux is constantly diffusing (by numerical diffusion working in consort with the shear forces) into

the surrounding accretion flow. Consequently, as the buoyant flux tubes spiral outward the field strength weakens considerably as the flux mixes back into the accretion flow in frames 6-10. This temporal evolution is repeated quasi-periodically. Similar cycles of vertical flux accretion/expulsion near black holes was anticipated in Punsly and Coroniti (1990) and is discussed in Chapter 8 of Punsly (2008).

### 3.3. Summary of Relevant Details

We summarize the key results from model-B of Igumenshchev (2008).

1. The time evolution of the vertical magnetic flux in 3-D is qualitatively different from that in 2-D .
2. In 3-D, strong patches of vertical magnetic flux form episodically and are located in the innermost regions of the accretion flow.
3. Plasma behaves as a two component system. There are the magnetic islands (strong magnetic field, low density regions) that tend to exclude the accretion flow (the 3-D version of a magnetically arrested accretion flow exists only locally). The second component is the bulk accretion flow in the form of spiral streams that "swims around" the magnetic islands by interchange instability.
4. The magnetic islands are not time stationary. They become buoyant and the flux is redeposited back into the outer accretion flow.
5. The spiral flow twists the vertical flux forming collimated bipolar Poynting outflows, or jets, that extract  $\sim 1\%$  of the binding energy of the accretion flow.

## 4. Vertical Magnetic Flux Near Rapidly Rotating Black Holes

In this section, we turn our attention to vertical magnetic flux evolution near a rapidly rotating black hole in the Kerr spacetime. The metric of the Kerr spacetime (that of a rotating uncharged black hole) in Boyer-Lindquist coordinates,  $g_{\mu\nu}$ , is given by the line element

$$ds^2 \equiv g_{\mu\nu} dx^\mu dx^\nu = - \left( 1 - \frac{2Mr}{\rho^2} \right) dt^2 + \rho^2 d\theta^2 + \left( \frac{\rho^2}{\Delta} \right) dr^2 - \frac{4Mra}{\rho^2} \sin^2 \theta$$

$$d\phi dt + \left[ (r^2 + a^2) + \frac{2Mra^2}{\rho^2} \sin^2 \theta \right] \sin^2 \theta d\phi^2, \quad (4-1)$$

$$\rho^2 = r^2 + a^2 \cos^2 \theta, \quad (4-2)$$

$$\Delta = r^2 - 2Mr + a^2 \equiv (r - r_+)(r - r_-). \quad (4-3)$$

There are two event horizons given by the roots of the equation  $\Delta = 0$ . The outer horizon at  $r_+$  is of physical interest

$$r_+ = M + \sqrt{M^2 - a^2}. \quad (4-4)$$

The stationary limit surface, at  $r = r_s$  occurs when  $\partial/\partial t$  changes from a timelike vector field to a spacelike vector field.

$$r_s = M + \sqrt{M^2 - a^2 \cos^2 \theta}. \quad (4-5)$$

This change happens when  $g_{tt}$  switches sign. The region in which  $g_{tt} > 0$  is the ergosphere. The outer boundary of the ergosphere is the stationary limit surface.

The lessons of the last section tell us that the time evolution of vertical magnetic flux near a black hole in 2-D and 3-D simulations can differ at the most fundamental levels. Thus, if we want to truly understand the properties of vertical flux distributions near black holes it is wise to work in 3-D. The only long term, high resolution, 3-D MHD numerical simulations in the Kerr spacetime are those developed in De Villiers and Hawley (2003a); De Villiers et al (2003b); Hirose et al (2004); Krolik et al (2005); Hawley and Krolik (2006); Beckwith et al (2008). There is no radiation term in the time evolution equations. Thus, as heat is generated, it can flow and be converted to gas pressure, but not to a flux of radiation. Thus, this is very different than a quasar.

The reader should refer to De Villiers and Hawley (2003a); De Villiers et al (2003b); Hirose et al (2004); Krolik et al (2005); Hawley and Krolik (2006); Beckwith et al (2008) to get more details on the many simulations that have been performed with this code over the years. This discussion is no more than a brief review. The initial state is a thick torus of gas in equilibrium that is threaded by concentric loops of weak magnetic flux that foliate the surfaces of constant pressure. The magnetic loops are twisted azimuthally by the differentially rotating gas. This creates significant magnetic stress that transfers angular momentum outward in the gas, initiating a strong inflow that is permeated with MRI driven turbulence. The end result is that after  $t =$  a few hundred  $M$  (in geometrized units), accreted poloidal magnetic flux gets trapped in the accretion vortex or funnel (with an opening angle of  $\sim 60^\circ$  at the horizon tapering to  $\sim 30^\circ - 35^\circ$  at  $r > 20M$ ). The orientation of the field in the funnel is the same as the leading edge of the poloidal loops in the initial state. The outer edge of the poloidal loops are initially driven outwards and never accrete within the

lifetime of the simulation. The strong transients die off by  $t = 2000 M$ , so the late time data dumps are the most physically relevant Hawley and Krolik (2006).

Numerically, the problem is formulated on a grid that is  $192 \times 192 \times 64$ , spanning  $r_{in} < r < 120M$ ,  $8.1^\circ < \theta < 171.9^\circ$  and  $0 < \phi < 90^\circ$ . Excision of the thin polar cone restricts the time steps to be not too small in the used spherical coordinates (the Courant condition) and greatly reduces the amount of computational resources required. The inner calculational boundary,  $r_{in}$ , is located close to, but just outside of the event horizon,  $r_+$ , where the Boyer-Lindquist coordinates are singular. The  $\phi$  boundary condition is periodic and the  $\theta$  boundary conditions are reflective. Zero-gradient boundary conditions are employed on the radial boundaries, where the contents of the active zones are copied into the neighboring ghost zones. MHD waves propagate slower than the speed of light, therefore the gravitational redshift creates a magneto-sonic critical surface outside of  $r_+$  from which no MHD wave can traverse in the outward direction Punsly (2008). The philosophy was to choose  $r_{in}$  to lie inside the magneto-sonic critical surface, thereby isolating it from the calculational grid. There are also steep gradients in the metric derived quantities as  $r_+$  is approached. This is handled by increasing the resolution of the grid near  $r_{in}$  with a "cosh" distribution of radial nodes.

We caution the reader that the results of these types of simulations are highly sensitive to the initial conditions that are imposed. Of all the loop configurations that are tried, only poloidal loops of the same orientation in a dipolar configuration produce strong Poynting jets. In Beckwith et al (2008), it was shown that if the loops are in a quadrupolar orientation in the initial state, the Poynting jet power coming from near the black hole is reduced to about 1% of the value obtained from the common orientation dipolar loops. If the loops are toroidal in the initial state, the Poynting jet power coming from near the black hole is reduced to about 0.1% of the value obtained from the common orientation dipolar loops. Finally, Beckwith et al (2008), showed that if the initial state of the torus is threaded by dipolar loops with more than one orientation, a strong Poynting jet only forms if a coherent packet of loops of like orientation accretes.

One of the highest spin simulations in this family is from Hawley and Krolik (2006) and is known as KDJ,  $a/M = 0.99$ . The last three time steps of KDJ with data collection were generously shared by J. Krolik and J. Hawley. Expressing the mass in geometrized units, the data dumps were performed at  $t = 9840 M$ ,  $t = 9920 M$  and  $t = 10,000 M$ . This complex simulation was crudely studied in Punsly (2007a,b). using 2-D visualization techniques. Due to the complex inhomogeneous nature the averages over azimuth that were employed did not yield a clear picture of the field configuration near the black hole. The purpose of this section is to use new 3-D visualizations techniques that allow us to clearly understand the varied

vertical flux structures that form near the rapidly rotating black hole in KDJ. It was pointed out in Punsly (2008), the unfortunate circumstance that all the plots from KDJ in Punsly (2007a,b) were displayed upside down. The north and south poles were reversed in all those plots, this is remedied here. The main emphasis in this study is to associate certain vertical field line topologies with the strong Poynting flux flares that emerge from the ergosphere in KDJ.

#### 4.1. The Poynting Jet in KDJ

The conservation of global, redshifted, or equivalently the Boyer-lindquist coordinate evaluated energy flux, defined in terms of the stress-energy tensor, is shown in Punsly (2007a) to simply reduce to

$$\partial(\sqrt{-g}T_t^\nu)/\partial(x^\nu) = 0 . \quad (4-6)$$

The four-momentum  $-T_t^\nu$  has two components: one from the fluid,  $-(T_t^\nu)_{\text{fluid}}$ , and one from the electromagnetic field,  $-(T_t^\nu)_{\text{EM}}$ . The quantity  $g = -(r^2 + a^2 \cos^2 \theta)^2 \sin^2 \theta$  is the determinant of the metric. The integral form of the conservation law arises from the trivial integration over Boyer - Lindquist coordinates of the partial differential expression (Thorne et al 1986). It follows that the the redshifted Poynting flux vector can be defined in Boyer-Lindquist coordinates as

$$\mathbf{S} = (S^r, S^\theta, S^\phi) = (-\sqrt{-g}(T_t^r)_{\text{EM}}, -\sqrt{-g}(T_t^\theta)_{\text{EM}}, -\sqrt{-g}(T_t^\phi)_{\text{EM}}) . \quad (4-7)$$

After averaging over azimuth, we use the poloidal projection of the Poynting vector,  $\mathbf{S}^P$ , to display the propagation of electromagnetic energy flux out of the ergosphere in KDJ. Consider figure 3, which is a false color plot of the azimuthal average of  $S^r$  at the three time steps. Notice that in each time frame, the flow of  $S^r$  across the white boundary (the stationary limit) is dominated by narrow channels that seem to initiate suspended outside the event horizon ( $r_+ = 1.175$  M) and the inner calculation boundary (shaded black) at  $r = 1.203$  M. In order to explain the origin of these energy beams, we overlay the direction of the poloidal Poynting vector in the each of the frames in figure 3. The white arrows represent the poloidal direction of the azimuthally averaged poloidal component of the Poynting flux,  $\mathbf{S}^P$ . The length of the arrows is proportional to the grid spacing and is not related to the magnitude of  $\mathbf{S}^P$ . The black contours on the plots are of the Boyer-Lindquist evaluated density, scaled from the peak value within the frame at relative levels of 0.5 and 0.1. The integral curves that are approximated by the white arrows show that the primary source of  $S^r$  is Poynting flux emerging from the accretion flow near the equatorial plane of the

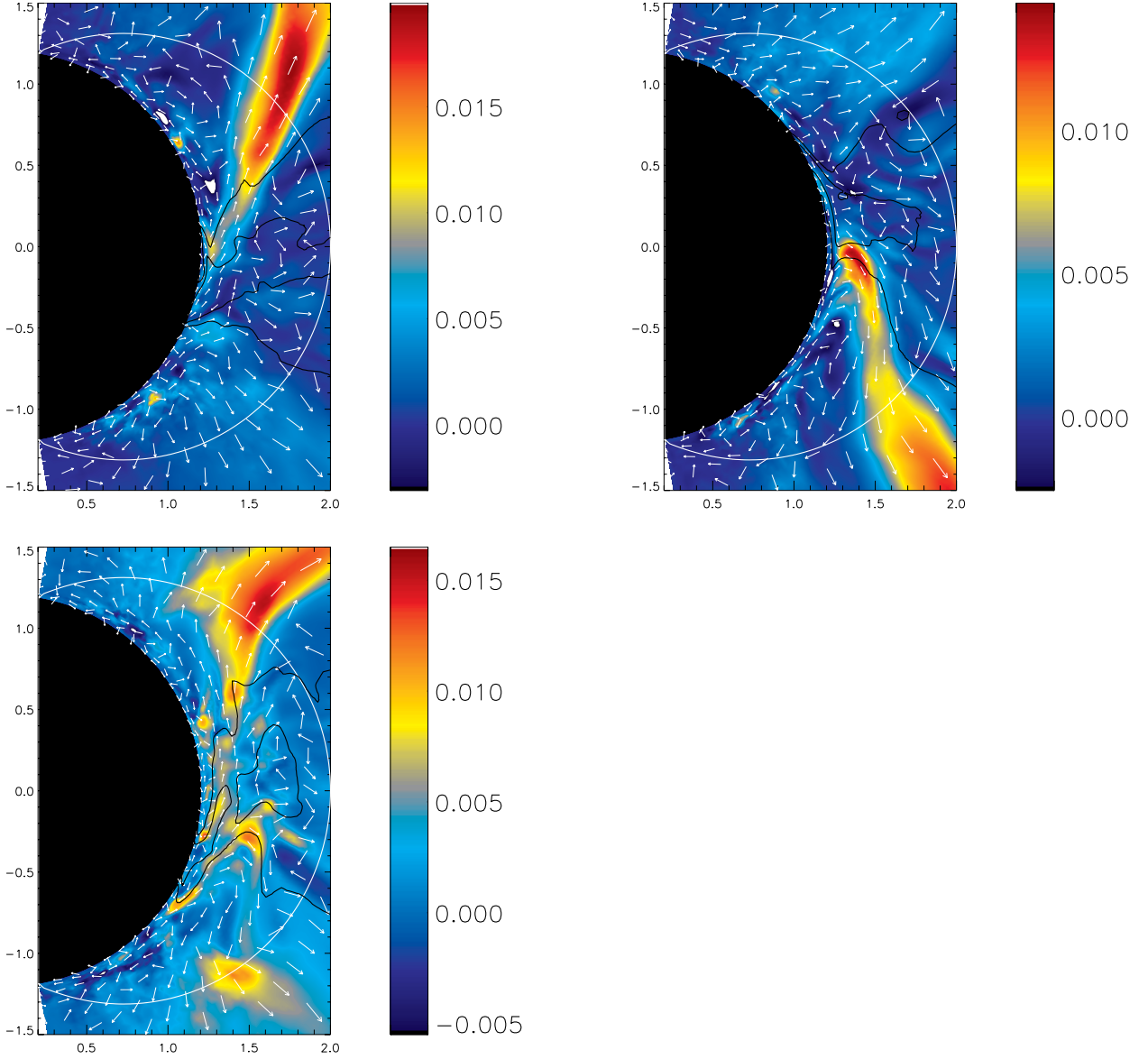


Fig. 3.— A false color plot of  $S^r$  averaged over azimuth at three time steps of KDJ,  $t = 9840$  M (top left),  $t = 9920$  M (top right) and  $t = 10000$  M (bottom row). The relative units (based on code variables) are in a color bar to right of each plot for comparison of magnitudes between the plots. Superimposed are white arrows that represent the direction of the azimuthally averaged poloidal component of the Poynting flux,  $\mathbf{S}^P$ . The length does not represent the strength of the poloidal Poynting flux, but is proportional to the grid spacing. The white contour is the stationary limit surface. The black contours on the plots are the Boyer-Lindquist evaluated density, scaled from the peak value within the frame at relative levels 0.5 and 0.1. The inside of the inner calculational boundary ( $r=1.203$  M) is black. The calculational boundary near the poles is at  $8.1^\circ$  and  $171.9^\circ$ . There is no data clipping, so saturated regions appear white.



ergosphere in all three frames. The direction of the white arrows indicate that  $\mathbf{S}$  has a large  $S^\theta$  component at its point of origin near the equatorial plane. Note that the energy conservation law in equation (4.6) is dominated by the electromagnetic terms for the energy flux emitted from the ergosphere (the mechanical energy flux is  $\sim 1\%$  -  $5\%$  of the electromagnetic energy flux emerging from the ergosphere). In Punsly (2007a), it was shown that there is a strong vertical magnetic field component at these locations as well. In this article, we actually create 3-D plots of the field lines to show the connection between field line topology and the creation of ergospheric Poynting flux in KDJ. We explore the possible vertical field configurations by studying each time slice individually.

The data presented in figure 3 is used to determine the relevant field lines to plot in 3-D that are required to elucidate the origin of the dominant component of the Poynting flux emerging from the ergosphere in KDJ, namely from the accretion flow near the equatorial plane. If we naively integrate field lines from random points, one gets a clutter of field lines that wrap around the black hole many times. It is impossible to extract the source of the strong Poynting jet from inner edge of the ergospheric accretion flow in the midst of this clutter. Our desire is to find the field lines that support this Poynting jet. We are not interested in plotting the field lines that seem to spiral endlessly in the equatorial plane and never connect to a jet. This will just mask the base of the ergospheric Poynting jet. Furthermore, the field lines that support the weaker Poynting flux contribution associated with the horizon magnetosphere (the Blandford-Znajek) type field lines are also not the focus of this study. For the interested reader, we note that these field lines have already been plotted for similar simulations in Hirose et al (2004). The exposition of these field lines would also clutter our view of the source of the dominant component of the ergospheric Poynting jet. Our final plots will have a wealth of detail as is. Thusly motivated, based on figure 3, we restricted the latitude of the starting points of field line integration to  $\pm 4^\circ$  of the equatorial plane and the interval,  $1.3M < r < 1.6M$ . This choice of integration starting points captures the poloidal magnetic flux that is contained within the dominant component of the ergospheric Poynting jet.

## 4.2. The time-slice $t = 9840 M$

This section begins our detailed study of the vertical flux in KDJ using 3-D visualization. The data from each time slice is presented in chronological order. The first time slice to be presented is at  $t = 9840 M$ . This time slice shows most of the features that were observed in the cumulative data from KDJ. It is perhaps the richest in terms of the variety of magnetic features and it is fortuitous starting point for our work.

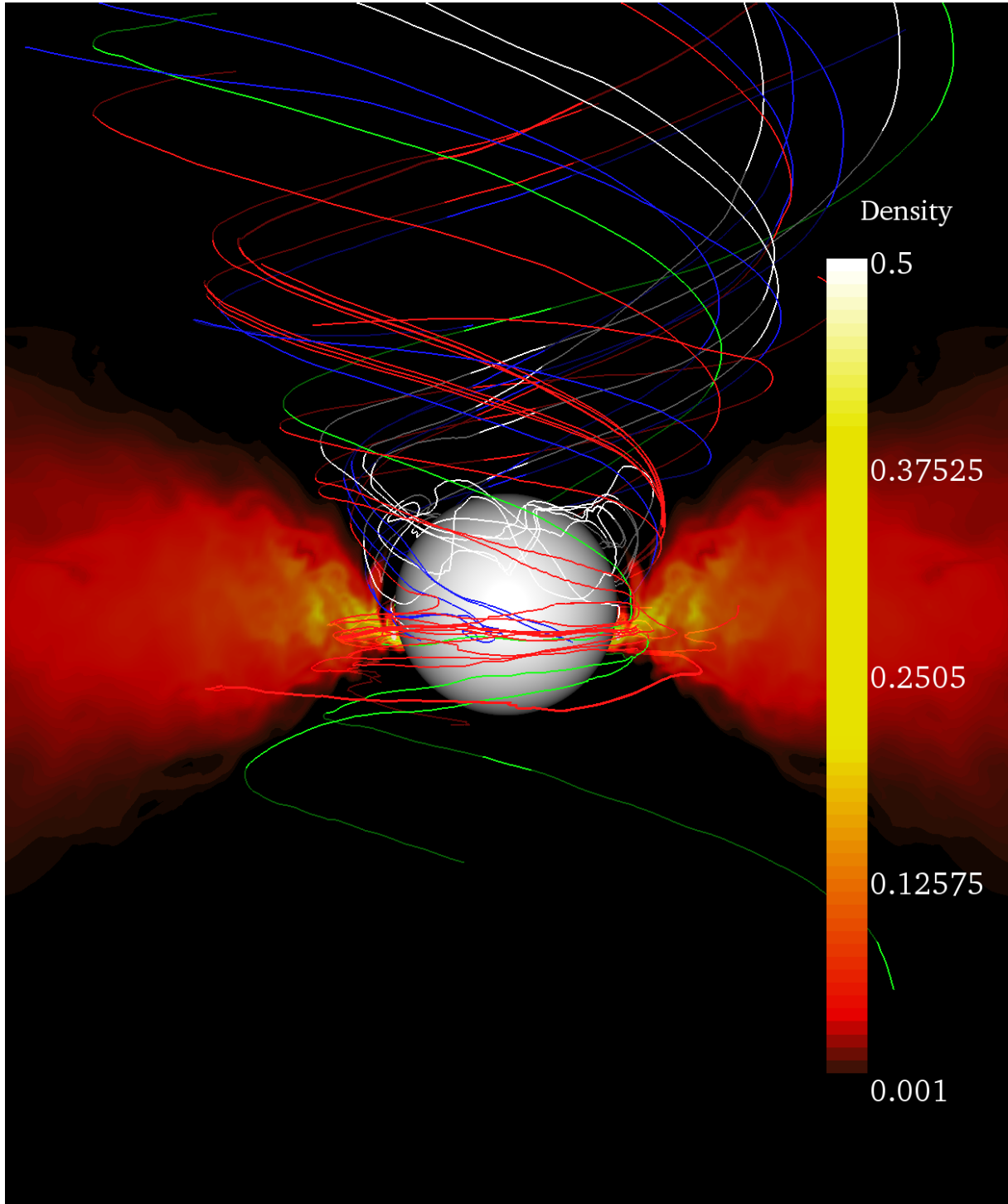


Fig. 4.— Magnetic field lines superimposed on the false color plot of Boyer-Lindquist evaluated density in a cross-section within the plane that is perpendicular to the line of sight. The values of the density are designated by the color bar in code units on the right hand side of the figure. The inner calculational boundary is shaded grayish-white for maximum contrast. The jet emerges from inner edge of the equatorial accretion flow.

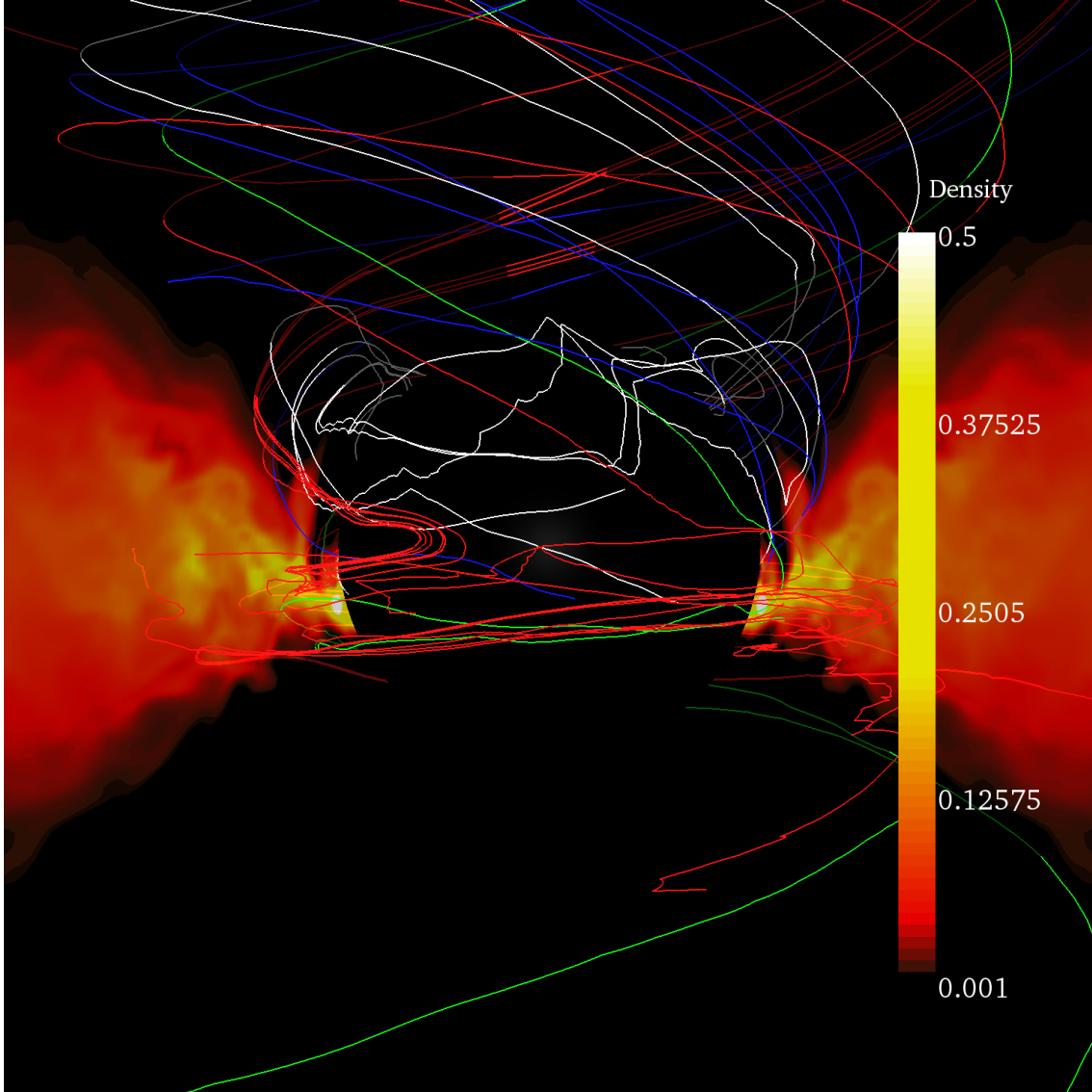


Fig. 5.— Magnetic field lines superimposed on the false color plot of Boyer-Lindquist evaluated density in a cross-section defined by the plane that is perpendicular to the line of sight. The values of the density are designated by the color bar in code units on the right hand side of the figure. The black hole is black. The jet emerges from inner edge of the equatorial accretion flow. In this figure, the camera in Paraview is rotated  $180^\circ$  in azimuth relative to figure 4. It is a closeup that highlights the interaction of the field lines and the accreting gas seen in cross-section. The inner calculational boundary is shaded black.

#### 4.2.1. *The Poynting Jet at $t = 9840 M$*

Figure 4 is a wide angle view of field lines that were integrated with Paraview 3.3.0 per the methods in the Appendix at the data dump corresponding to the Boyer-Lindquist time,  $t = 9840 M$ . The Paraview camera in figure 4 is positioned in the equatorial plane. Figure 5 is a closeup of the same 3-D geometry that exists at  $t = 9840 M$ , viewed along the equatorial plane. The camera in Paraview is rotated  $180^\circ$  in azimuth in figure 5 relative to figure 4. The advantage of the closeup is to highlight the interaction of the field lines and the accreting gas seen in cross-section. The advantage of the wide angle view is to highlight the large scale jet. The backgrounds of figures 4 and 5 are false color contour maps of a 2-D cross-section of the Boyer-Lindquist evaluated density in the plane that is perpendicular to the line of sight. The values of the density are designated by the color bar in code units on the right hand side of the figure. The interior of the inner calculational boundary is shaded grayish-white in figure 4 for maximum contrast. The interior of the inner calculational boundary is left black in the closeup view presented in figure 5. The density is chosen with an opacity of 80% so that field lines can be seen penetrating the accreting gas from the back side to the front. Consequently, when the field lines are on the back side of the plane of the figure they appear darker, this makes it easier to visually trace out the spirals of the magnetic field in the jet. If the opacity of the density cross-section were chosen to be 100% then the field lines would be completely obscured on the back side. Recall that the polar regions within  $8.1^\circ$  are excised for computational efficiency. Thus there is no data (including gas density) in this region. Consequently, every time a field line on the back side crosses these polar regions it suddenly becomes as vivid as the near side part of the field line (there is nothing that is opaque that blocks our view).

The origin of the preponderance of the Poynting flux at  $t = 9840 M$  (the narrow red channel in the top left frame of figure 3) is almost completely obscured by a tangle of field lines, many that wrap around endlessly in the equatorial accretion flow. From the top left frame of figure 3, it is clear that the strong narrow channel that dominates the northern Poynting jet originates from near the equatorial plane at  $r < 1.55M$ . This is the region that is relevant to our study and the field lines in figures 4 and 5 were chosen accordingly. In order to produce figures 4 and 5, we selected 60 starting points for the field line integrations as follows. First of all, we restricted the latitude of the starting points of integration to  $\pm 4^\circ$  of the equatorial plane. With this restriction on latitude, we chose 40 points at random from the interval,  $1.35M < r < 1.55M$ , and an additional 20 starting points for integration were chosen randomly from the interval,  $1.30M < r < 1.60M$ . The field lines were integrated in both directions. The integrations were terminated if the field line penetrated the computational boundaries. We used 1000L steps per integration of field lines of length L in units of the geometrized mass. Increasing this to 10000L steps in the

Runge-Kutta integration method showed only minor differences. Thus, we concluded 1000L steps were sufficient in the integration routine. Each field line was integrated 3 times, with lengths,  $L$ , of 10M, 20M and 100M. Varying  $L$  on a case by case basis was advantageous for increasing the clarity of display in the figures. Ideally, having all the lines at 100 M is best for seeing the jet. But many of the field lines in the jet coil endlessly at their base within the accretion flow (in particular the type I lines that are discussed in detail below). The coiling in the accretion flow blocks off and confuses any details of the other interactions of the field lines with the accreting gas. Ultimately, it is just an incomprehensible mess of toroidal coils. For these types of field lines, we typically chose a length of 20 M for display purposes. This ended up creating a little more than one toroidal circuit in the accretion flow (this is why the type I field lines in some of the wide angle views don't extend as far into the jet as the other field lines that are integrated to a length of 100 M).

Out of the 60 starting points, 22 of the field lines that were generated connected to the bipolar Poynting jets. Most of the others were predominantly toroidal in nature and did not connect to the Poynting jet. Some of these toroidal loops seemed to spiral endlessly near the black hole. Others passed through the equator and spiraled outward in the accretion flow into the opposite hemisphere. Others crossed the equatorial plane and spiraled out into the corona above the disk into the opposite hemisphere, propagating to large distances, but never actually merging with the Poynting jet. These predominantly toroidal field lines obscured the base of the vertical field lines that did join the Poynting jet, so they were omitted from figures 4 and 5 since they do not shed light on the topic at hand, but actually hide interesting details from view. There were also a few loops that came out of the inner calculational boundary then intersected the accretion flow and finally closed on the inner calculation boundary at high latitude. This was only time slice in which such loops were prevalent.

The field lines were color coded in figures 4 and 5 for the discussion of the taxonomy of vertical field lines in the next subsection. To our surprise, the vertical flux through the equator is not a single type of field line, but we have discovered 4 different types of vertical field lines near the equatorial plane that comprise the large scale jet. The coiling in the field lines indicates that there is a Boyer-Lindquist evaluated magnetic field component,  $B^\phi$ , in the compact notation of equation (A.7). Also, since there is a non-zero pitch angle to the large scale field, there is a poloidal magnetic field component in the low density polar region of figure 4,  $\mathbf{B}^{\mathbf{P}} \equiv (B^r, B^\theta)$  in the notation of equation (A.7). Since it was shown in Punsly (2007a) that the field lines at the base of the jet at  $t = 9840$  M, rotate with an angular velocity that is approximately that of the event horizon,  $\Omega_F \approx \Omega_H$ , in the Boyer-Lindquist coordinates, there is an associated motional, poloidal (cross-field) EMF,  $\mathbf{E}^{\mathbf{P}} \sim \Omega_F (B^\theta, -B^r)$ . Consequently, there is a poloidal Poynting vector  $\mathbf{S}^{\mathbf{P}} \sim \mathbf{E}^{\mathbf{P}} \times B^\phi \mathbf{e}_\phi \sim (\Omega_F F_\phi^\theta F_{\theta r}, \Omega_F F_\phi^r F_{\theta r})$ ,

where the covariant Boyer-Lindquist basis vector  $\mathbf{e}_\phi$  is the coordinate vector field  $\partial/\partial\phi$  (Punsly 2008). Thus, the existence of rotating, coiled field lines in the accretion vortex is equivalent to a Poynting flux jet. Notice that the twisted field lines in figures 4 and 5 exit the accreting gas at roughly the same place that the narrow, strong channel of poloidal Poynting flux emerges from the azimuthally averaged image in the top left frame of figure 3. These 3-D coiled field lines explain why the white arrows (Poynting vector) in the top left frame of figure 3 come out of the inner regions of the accretion flow. In Punsly (2007a) and in Chapter 11 of Punsly (2008) it was shown that the Poynting jet that is driven from the inner edge of the accretion is tantamount to the high accretion rate analog of the "ergospheric disk" jet that was first described in Punsly and Coroniti (1990).

#### 4.2.2. Vertical Field Line Taxonomy

We now describe the different types of vertical field lines that were found and motivate the distinct designations that were assigned by defining characteristics that distinguish each type. In all of the figures that display the magnetic field lines in KDJ in this paper, the poloidal field goes from the northern hemisphere towards the southern hemisphere (correcting the mistake that the field lines point from south to north in Punsly (2007a,b)). Consequently, we did not include arrows on the field lines because they added additional clutter to the already complex, very inhomogeneous environment. The vertical field line categories are labeled type I - type IV. The type I - type III field lines are illustrated explicitly in figures 6 - 8, respectively.

##### *Type I Field Lines*

These field lines are distinguished by connecting to the Poynting jet in one hemisphere only, with the other end spiraling around within the accreting gas in the opposite hemisphere (see figure 6). Another distinguishing feature of the type I field lines is that the azimuthal direction of the magnetic field changes direction as the field line crosses the midplane of the accretion flow. Figure 6 is viewed along the equatorial plane with the Paraview camera positioned at an azimuth similar to its location in figure 5. Half of the jet field lines from the inner accretion flow at  $t = 9840 M$  (11 out of 22) are this type in figures 4 and 5 (note that the frequency of occurrence of a type of field line does not equate to a magnetic field strength). In this time step, type I field lines are the most common variety in the ergospheric disk jet. They are color coded in red in the figures throughout this article. The "anchoring" end of the field line spirals just below the equator near the black hole for many revolutions, then spirals out into the distant reaches of the corona or accretion disk proper within the

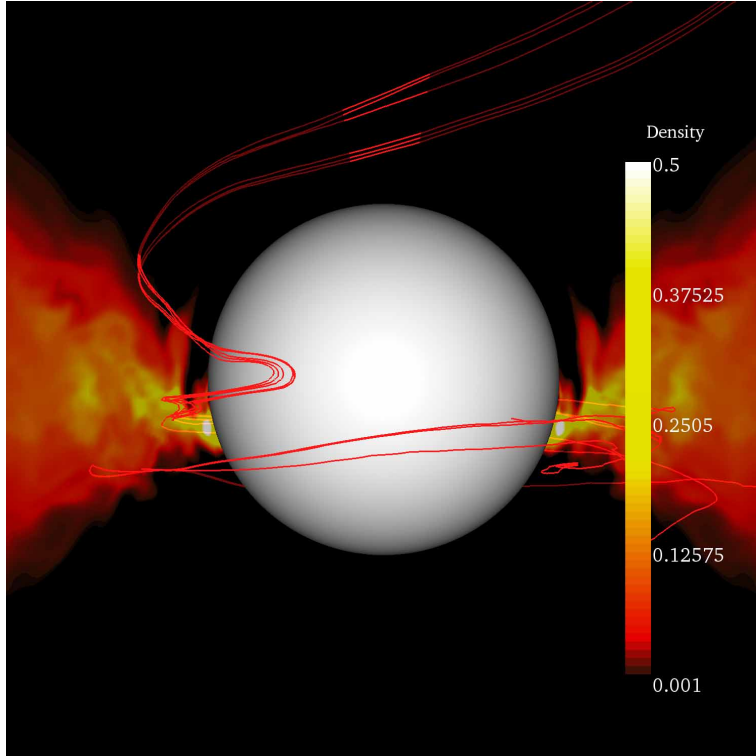


Fig. 6.— The type I vertical magnetic field lines that emerge from the inner equatorial accretion flow. The false color plot is a contour map of a 2-D cross-section of the density in Boyer-Lindquist coordinates expressed in code units. The interior of the inner calculation boundary is grayish-white. These field lines are distinguished by connecting to the Poynting jet in one hemisphere only, with the other end spiraling around within the accreting gas in the opposite hemisphere. Another distinguishing feature of the type I field lines is that the azimuthal direction of the magnetic field changes direction as the field line crosses the midplane of the accretion flow.

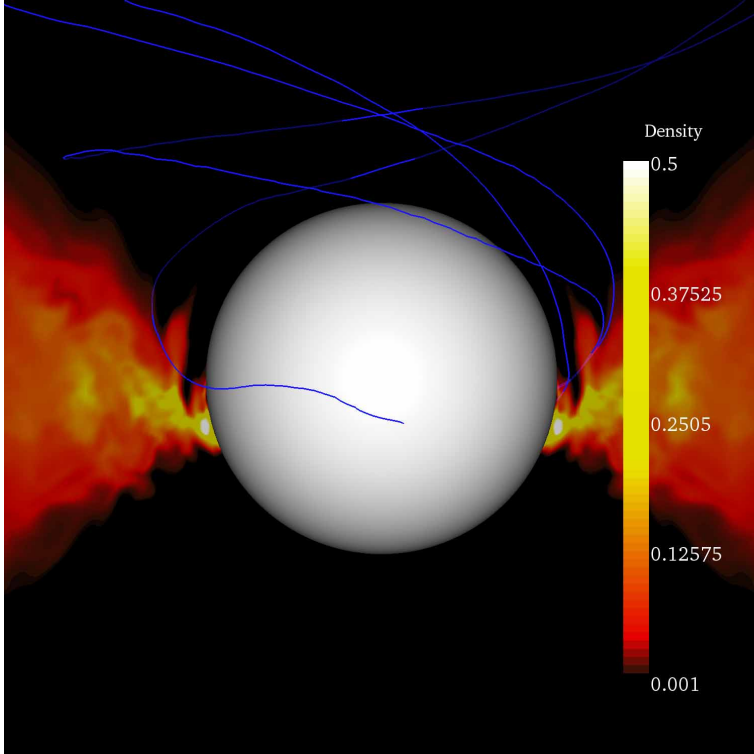


Fig. 7.— The type II vertical magnetic field lines that emerge from the inner equatorial accretion flow. The false color plot is a contour map of a 2-D cross-section of the density in Boyer-Lindquist coordinates expressed in code units. The interior of the inner calculation boundary is grayish-white. The type II field lines intersect the inner calculational boundary. They traverses the lateral extent of the accretion flow, connecting the jet in one hemisphere to their point of origin on the inner calculational boundary in the opposite hemisphere. Notice that the type II field lines interact mainly with the less dense regions (typically, 1% - 10% of the peak density) of the accretion flow.



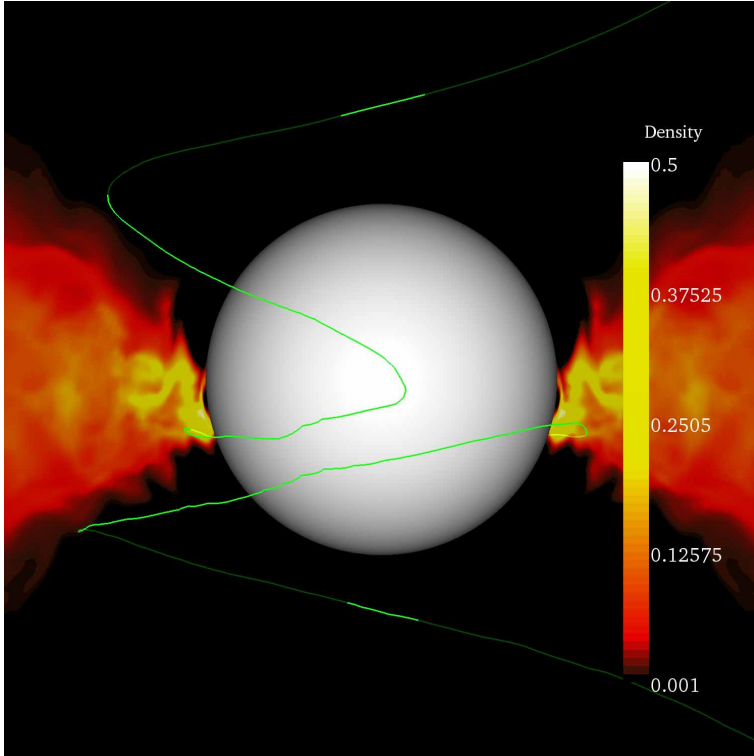


Fig. 8.— The type III vertical magnetic field lines emerges from the inner equatorial accretion flow. The false color plot is a contour map of a 2-D cross-section of the density in Boyer-Lindquist coordinates expressed in code units. The interior of the inner calculation boundary is grayish-white. The type III field lines connect to both sides of the bipolar jet. Like the type I field lines the azimuthal direction of the magnetic field changes direction as the field line crosses the midplane of the accretion flow.

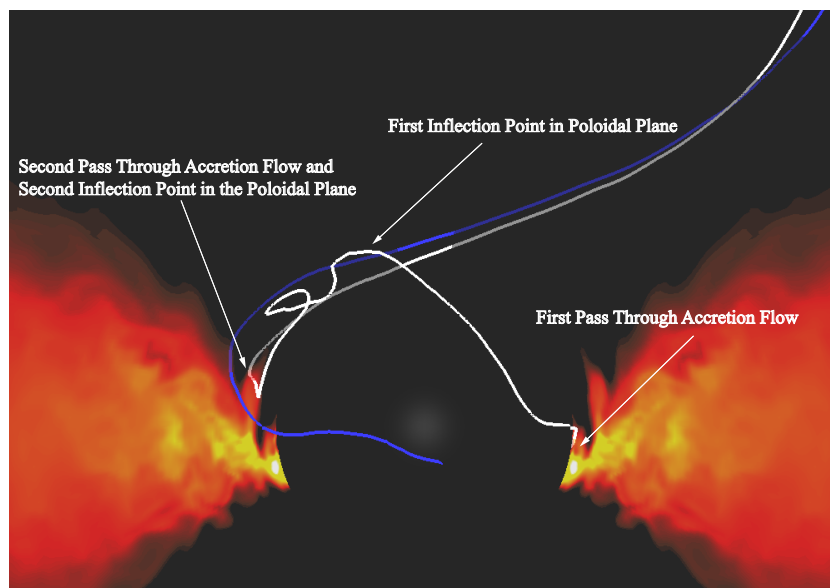


Fig. 9.— A type IV field is shown in white. The false color plot is a contour map of a 2-D cross-section of the density in Boyer-Lindquist coordinates. The interior of the inner calculation boundary is black. This figure compares and contrasts the type IV and type II field lines (shown in blue for comparison). These field lines are from figures 4 and 5, but they have been individually rotated in azimuth by different amounts for illustrative purposes. Thus, there is no physical connection between the density contours and the individual field lines. Both field lines intersect the inner calculational boundary. The type IV field line intersects the boundary at a slightly higher latitude than the type II field line. The initial integration away from the inner calculational boundary proceeds similarly, both field lines increase in latitude as they spiral around the black hole, exiting the accreting plasma. The type II field line is at slightly larger radius and connects directly into the jet once it exits the accreting plasma. By contrast, the type IV field line experiences an inflection in the poloidal plane and bends back down towards the accretion flow. The field line continues its spiral around the black hole dipping into the upper layers of the accretion flow one more time, at a larger radius than the first pass through the accretion flow. Within these upper layers it experiences a second poloidal inflection point and bends upward, finally merging with the Poynting jet.

hemisphere opposite the jet. Thus, the anchoring end of the field line becomes inextricably tangled with the other toroidal coils within the turbulent region of the accretion flow. This field line topology was never envisioned in theoretical work. Dynamically speaking, the most important feature of the type I field lines in figure 6 is that the azimuthal direction of the magnetic field changes direction as the field line crosses the midplane of the accretion flow. This type of magnetic field polarization reversal is associated with an Alfvén mode in MHD and is sometimes called an Alfvén rotation (Kantrowitz and Petschek 1966). The type I field lines are a conduit for powerful Alfvén waves to radiate from the accretion flow into the jet within the accretion vortex.

### *Type II Field Lines*

The type II field lines originate from the inner calculational boundary. They traverse the lateral extent of the accretion flow, connecting the jet in one hemisphere to their point of origin on the inner calculational boundary in the opposite hemisphere. This class of vertical field line was never anticipated theoretically. They are depicted with the examples extracted from time step  $t = 9840$  M in figure 7. This is the second most common type of field line in the ergospheric disk jet at  $t = 9840$  M in figures 4 and 5 (6 out of the total of 22 field lines). However, considering all three time snapshots to be discussed, it is the most common, 29 out of the total of 63 ergospheric disk jet field lines that are plotted in this section (see the discussions in subsections 4.3 and 4.4). The false color contour plots of the density in figures 4, 5 and 7 indicate that the type II field lines (color coded blue) interact mainly with the less dense regions (typically, 1% - 10% of the peak density) of the accretion flow. The interaction of the field lines with the accreting gas creates outgoing Poynting flux that is transmitted along the poloidal field lines from the accreting gas into the jet.

### *Type III Field Lines*

The type III field lines (color coded green) connect to both halves of the bipolar jet (see figure 8). The type III field line that is illustrated in figure 8 was extracted from the jet in figures 4 and 5. This was the type of vertical field line that had been expected to occur in equatorial accretion flows near black holes in simplified theoretical discussions (Thorne et al 1986; Punsly and Coroniti 1990; Punsly 2008). Surprisingly, this turns out to be the rarest type of field line that we encountered in KDJ. Only 2 out of 22 jet field lines were of this type at  $t = 9840$  and only 6 out of 63 in all three time slices combined. Like the type I field lines, the azimuthal field direction switches sign within the accretion flow near the equatorial plane (the Alfvén mode polarization of MHD). The scarcity of type III field lines is intimately related to the fact that the ergospheric disk jets form asymmetrically in KDJ.

In all three time slices, one jet (at  $t = 9840 M$  it is clearly the northern jet) is much more powerful than the other. We have color coded the type III field lines as green throughout. We note that the 3-D numerical simulations of the relativistic string approximation to thin magnetic flux tubes around rapidly rotating black holes in Semenov et al (2004) produced type III field lines exclusively.

In figure 8, the Paraview camera is rotated  $70^\circ$  about the black hole rotation axis relative to figures 5-7. Notice that the gas density in the inner regions of the cross-section is considerably larger than in figures 6 and 7. The accretion flow is clearly nonuniform in azimuth. Similar dense "fingers" of accreting gas also occurred in the 3-D numerical simulations of Igumenshchev (2008) as exemplified by the even columns of figure 2. This appears to be an endemic feature of 3-D accretion in the presence of vertical flux, since similar "tongues" of dense plasma occur in 3-D MHD simulations of gas accreting onto highly magnetized stars (Romanova et al 2008).

#### *Type IV Field Lines*

The type IV field lines follow a circuitous path from the inner calculational boundary to the jet. Ostensibly, the integral curves near the inner calculational boundary seem to be on a trajectory that will either promptly merge with the jet after passing through some accreting gas (just like the type II field lines) or they might seem to be destined to link the horizon to the jet directly (like a Blandford-Znajek type field line). However, instead of a direct path to the jet, the type IV field lines are diverted back towards the accretion flow (This is explicitly demonstrated by figure 9 which contrasts a type IV field line with a type II field line). The type IV field lines are characterized by this inflection point in the poloidal plane. These field lines bend back towards the accretion flow, penetrating the surface layer of the inner edge of the accretion flow, then "reflect" out of the accreting flow into the jet. The inner portion of the field line is effectively one half of a magnetic field loop, either connecting the innermost accretion flow to a more distant part of the accretion flow, or connecting the inner calculational boundary to the accretion flow. But instead of the magnetic loops closing, the field lines are redirected back out of the accretion flow into the jet - in the same hemisphere that contains the "half-loop". Thus they have two inflection points in the poloidal plane. The first bends the field line from above the accretion flow down into the accretion flow. The second inflection point bends bends the field line out of the accretion flow into the Poynting jet. The multiple inflection points make these the most complicated field lines that are considered. The type IV field lines (color coded white) in figures 4 and 5, propagate outward from the inner calculational boundary, but are corralled by a wall of type II field lines. Visually, it appears that this is related to the inflection point that bends the type IV

field toward the accretion flow. The type IV field lines gradually (sometimes after more than one revolution about the black hole) work their way through gaps in the type II magnetic wall at  $t=9840$  M. The multiple inflection points and the fact that they traverse one or more complete circuits about the black hole, make the type IV field lines the most difficult to visualize without a fluid camera angle.

#### 4.2.3. *Animations Reveal a Complicated Layered Magnetosphere*

Every line of sight has hidden features in 3-D. Clearly there are dynamically important features in figure 5 within the accretion flow that can not be seen in figure 4. Animations of the camera rotating around the black hole are the best way to visualize these complex 3-D magnetospheres. Thus, we have supplied an animation of the camera rotating counter-clockwise about the black hole spin axis (the vertical axis in figures 4 and 5) with the line of sight restricted to the equatorial plane (as in figures 4 and 5), designated as movie 2 in the on-line material. The first frame of this animation is given in figure 10. In order to keep the gas semi-transparent, we have plotted the density a bit differently in the animation than was done in figures 4 and 5. For the sake of maximum clarity, we have plotted three, 3-D, contours of the Boyer-Lindquist density superimposed on each other. One contour level is at 0.05 in code units and is plotted with 40% opacity, the next is at 0.1 with 35% opacity and the third contour level is at 0.15 and it is plotted at 30% opacity. Three, 3-D contours surfaces and this level of transparency gave the best balance between seeing the gas and seeing field lines within the gas in our opinion. We only plot one of the type IV field lines because a plot of all 4 such field lines circling the black hole blocks our view of the other field lines in the jet. Unfortunately, the transparency of the gas in the animation is not readily apparent in the print version of the first frame (figure 10). The back illumination of the images that are provided by a computer screen enhances the transparency of the translucent gas contours.

Movie 2 and figure 10 are useful for seeing the jet emerging from the accreting gas. However, this equatorial line of sight obscures the interplay between the base of the jet field lines and the accreting gas. The maximum amount of clarity is given by the "isometric view" (a line of sight that is 30 degrees above the equatorial plane). This view allows for a clear line of sight towards the interaction of the base of the field lines that comprise the jet with the accreting gas (see movie 3 and figure 11). The jet can still be seen, but many of the coiled jet field lines attain peculiar shapes due to the off-angle perspective. From this angle, it would be hard to realize that the northern jet is conical as is obvious in movie 2 (figure 10). Figure 11 is the first frame of movie 3, the isometric view. In movie 3, the Paraview camera

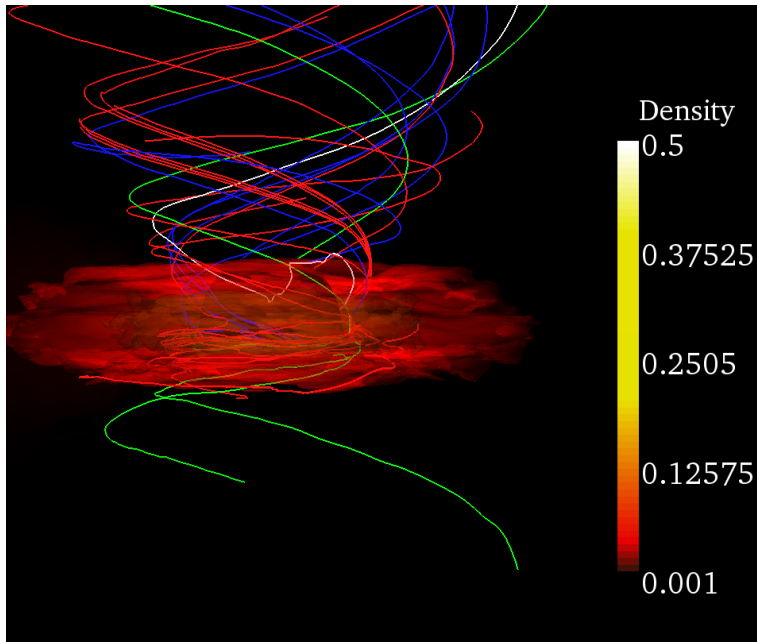


Fig. 10.— The first frame of movie 2. The false color background is comprised of three 3-D contours of the Boyer-Lindquist density superimposed on each other. One is at 0.05 in code units and is plotted with 40% opacity, the next contour level is at 0.1 with 35% opacity and the third contour level is at 0.15 and it is plotted at 30% opacity. Notice that the white, type IV field line emerges from accreting gas on the right then bends down back into the accretion flow briefly in the front before joining the jet. This second encounter with the accretion flow is the defining characteristic of type IV jet field lines.

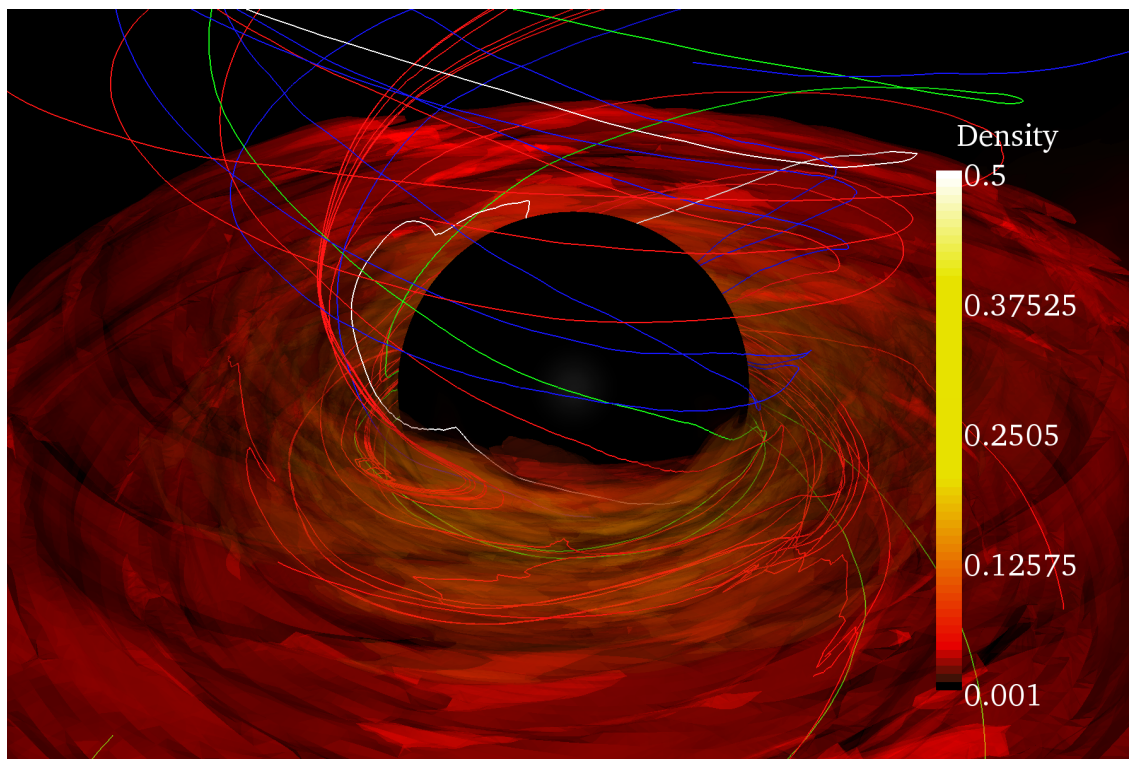


Fig. 11.— The first frame of "isometric view" movie 3. The false color background is comprised of three 3-D contours of the Boyer-Lindquist density superimposed on each other. One is at 0.05 in code units and is plotted with 40% opacity, the next contour level is at 0.1 with 35% opacity and the third contour level is at 0.15 and it is plotted at 30% opacity.

swings around the black hole rotation axis in the counter-clockwise direction, all the time maintaining a latitude of  $30^\circ$  above the equator. The false color background is comprised of three 3-D contours of the Boyer-Lindquist density superimposed on each other at the same levels and opacity as figure 10 (movie 2). Again, for the sake of clarity, we plot only one of the type IV field lines. The value of the gas density in regions of the accretion flow that are threaded by jet field lines is more readily apparent in movie 3 than in figure 11. This is an example of how a fluid camera angle is vastly superior to simple snapshots and slices for clarifying complicated structures. As the camera angle starts to rotate in movie 3, one can see that a cluster of type I field lines, just to the left of center. At this camera angle and in figure 11, it appears as if the cluster of type I field lines is embedded within a "finger" of the higher density gas. However, during the time interval 5 to 7 seconds in movie 3, it is revealed that the field lines actually reside in a low density cavity that is adjacent to this "finger" of dense gas. From the isometric perspective in figure 11 and movie 3, it is clear that all of the jet field lines emerge from the accreting gas and do not go straight from the event horizon into the jet as proposed in the model of Blandford and Znajek (1977). The existence of a significant number of these jet field lines (that do not go directly from the horizon to jet) is in contradistinction to the findings of Hirose et al (2004) that such field lines do not exist in the particular 3-D simulation that they studied in detail.

Our detailed study of the field line types in the animations indicate the basic following structure of the inner disk magnetosphere at  $t = 9840 M$ . The inner-most jet field lines from the ergospheric accretion flow are type IV. Just outside of these, the type II field lines appear to thread the gas in an irregularly shaped inner edge (or boundary layer) of the accretion flow that angles across the equatorial plane. In figures 4, 5 and 7, it is clear that the type II lines intersect the accretion flow in regions on the north face where the density is only about 1% - 10% of the density peak. The strongest azimuthally averaged poloidal field strength in this time slice is within the base of the jet emerging from the ergospheric accretion flow. The magnetic pressure of these field lines is so large that it is apparently redirecting the accreting gas to flow predominantly below the equatorial plane as it approaches the inner calculational boundary. In figure 11 (and movie 3), just outside of the type II lines are the type I lines. As discussed above, in figure 11 (and movie 3), we can see that the type I field lines carve out low density cavities ( $\sim 10\%$  of the peak density) within the accreting gas above the midplane. Finally, the type III field lines seem to be located the farthest out in the accretion flow at  $t = 9840 M$ , but this conclusion is based on only two type III field lines.



#### 4.2.4. Magnetically Arrested Accretion in 3-D

There is clearly a strong interaction between the magnetic pressure from the vertical flux forming the base of the jet and the accreting gas. We explore this interface and its relationship to magnetically arrested accretion that was discussed in the context of simulations in the Pseudo-Newtonian potential in section 3. Figure 12 is an ambitious attempt to capture three dynamical entities in one figure, the "streamlines" of the accreting gas, the magnetic field lines and the density. Unfortunately, the complicated 3-D dynamics requires a complex figure and Paraview 3.3.0 gives us the visualization tool to create relatively easy to understand images. In figure 12, the Boyer-Lindquist evaluated gas density is seen in cross-section by means of a false color contour map. The color bar on the right hand side of the figure is in code units and the scale was optimized to give the best contrast between the field lines, the accretion flow gas density and the background. The magnetic field lines were chosen to lie within the magnetic wall located near the inner edge of the northern side of the accretion disk. They were preferentially selected to intersect the gas in the plane of the image. The magnetic wall that is referred to here is the same as the magnetic wall that was discussed in subsection 4.2.2. This choice of plotting preferences has the tremendous advantage that one can see the density of the gas in which the magnetic wall is embedded. In order to elucidate the structure of the magnetic wall, the opacity of the gas was chosen to be relatively high (85%), so that it was obvious when the field lines penetrated the gas within the cross-sectional slice. In particular, the field lines comprising the magnetic wall on the left hand side of figure 12, suddenly almost completely disappear when they intersect the red false color gas density contour. On the left hand side, we see a strong magnetic wall of type II field lines. On the right hand side, the magnetic wall appears to be a roughly equal mix of type I and type II field lines. They overlay almost on top of each other, so the red and blue meld into a maroon color.

On the backdrop of the magnetic wall and the accretion flow, we plotted two streamlines of the accreting gas defined as the integral curves of the velocity (the analogs of equations A.16 - A.18),

$$\frac{dx}{ds} = \frac{(v^r) \sin \theta \cos \phi + (rv^\theta) \cos \theta \cos \phi - (r \sin \theta v^\phi) \sin \phi}{\|v\|} \quad (4-8)$$

$$\frac{dy}{ds} = \frac{(v^r) \sin \theta \sin \phi + (rv^\theta) \cos \theta \sin \phi + (r \sin \theta v^\phi) \cos \phi}{\|v\|} \quad (4-9)$$

$$\frac{dz}{ds} = \frac{(v^r) \cos \theta - (rv^\theta) \sin \theta}{\|v\|} \quad (4-10)$$

$$\|v\|^2 \equiv g_{rr}v^{r2} + g_{\theta\theta}v^{\theta2} + g_{\phi\phi}v^{\phi2}, \quad (4-11)$$

where,  $v^r = dr/dt$ ,  $v^\theta = d\theta/dt$  and  $v^\phi = d\phi/dt$ . It is important to clarify for the reader

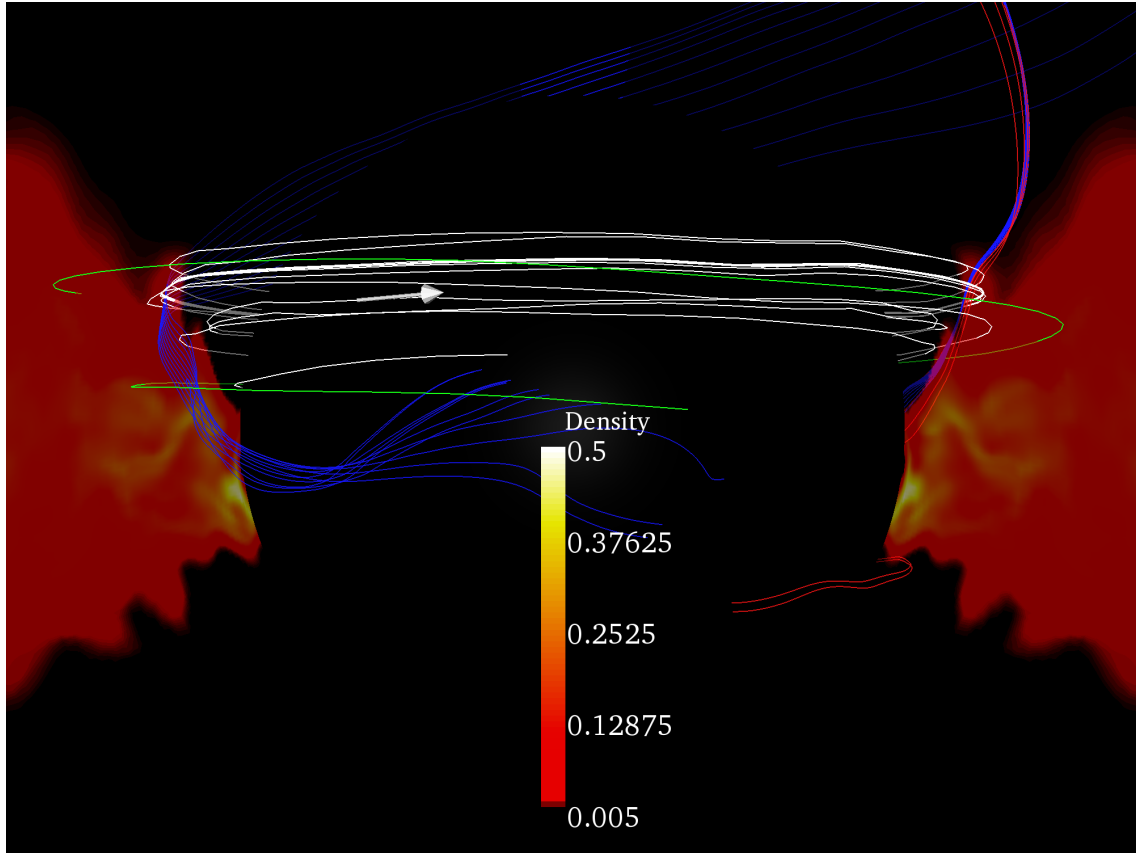


Fig. 12.— The 3-D version of magnetically arrested accretion. The white and green curves are integral curves of the Boyer-Lindquist evaluated velocity at  $t = 9840 M$ , gas streamlines. The false color contour map of a cross-section of the density is in code units. The blue and red curves are magnetic field lines with the color coding described in the text. The white curve is a magnetically arrested streamline. Notice that as the footpoint of the type II field lines on the inner calculational is displaced toward the north, the topology starts to deform toward that of the type IV field lines.

that these are not true streamlines in the time dependent sense. The green and white lines do not represent global trajectories into the black hole, since the vertical magnetic field is dynamic and therefore so are the magnetic forces in KDJ; the magnetic forces could be significantly altered after a few revolutions of the black hole. For this reason, the trajectories are only physically representative of the gas propagation in a local sense. We chose two starting points for the integration of the gas streamlines for illustrative purposes. The first integration resulted in the white integral curve that was selected because it was strongly perturbed from rapid radial in-fall at the location of the magnetic wall on the left hand side. We added only one arrow (to avoid clutter) to show the direction of motion in both streamlines. The white curve shows us two things. Notice that the integral curve seems to be closely aligned with the kinks seen in the magnetic wall. These kinks could represent local enhanced magnetic stresses that naturally arise when gravitational forces on the gas and pressure gradients within the gas are in opposing directions. Also notice that the accretion of the plasma that is represented by this streamline is clearly magnetically arrested. It takes many spirals around the black hole before it crosses the magnetic barrier by winding through small gaps and finally reaches the inner calculational boundary. To show that this streamline actually represents magnetically arrested gas, we plotted a "control" streamline in green. This streamline is chosen at a similar disk height, but farther out in the disk. It never strongly interacts with the magnetic wall. It reaches the inner calculational boundary at an azimuthal coordinate just beyond the "footpoints" of the magnetic wall, flowing always outside the magnetic wall. Thus, it flows toward the inner calculational boundary virtually unimpeded by any of the putative strong magnetic forces associated with the magnetic wall. The green streamline in figure 12 is typical of most streamlines in the body of the accretion disk and indicates that a direct inflow takes only  $\approx 1.5$  spirals to reach the inner calculational boundary, a much shorter journey than the white (magnetically arrested) streamline.

Even though the white streamline does not represent a global time dependent path for the gas (because of the vertical field and associated magnetic force variations noted above), it is indicative of a strong interaction all the along length of a slow inward spiral. The magnetic kinks and the low pitch angle spiral of the streamline are consistent with the notion that the gas is being held up by magnetic forces virtually everywhere all along the length of the streamline at the interface of the magnetic wall. The magnetically arrested property is depicted by figure 12, but the number of spirals around the black hole that it takes for a given fluid element to reach the black hole is not determined by this integration. Even though some gas is magnetically arrested, the majority of the accreting gas finds its way to the black hole by maneuvering around the strong patches of vertical flux, passing through the azimuthal gaps in the vertical magnetic flux distribution and the vertical gaps in the azimuthal twists in the type I field lines near the equatorial plane.

### 4.3. The time-slice $t = 9920 M$

The next time step in which data was dumped is at  $t = 9920 M$ . Unfortunately, this time slice is too distant in time from the  $t = 9840 M$  time slice data in order to define any continuous change in magnetospheric parameters ( $\gtrsim 6$  black hole rotational periods). The most surprising element of this time slice is that the stronger jet in figure 13 points to the south, the opposite of the case for  $t = 9840 M$ . The magnetospheric geometry at  $t = 9920 M$  is the least complex of any that is found in the three available time slices. Thus we only use 40 starting points for our field line integrations. The starting points of integration are restricted to  $\pm 4^\circ$  of the equatorial plane as before. With this restriction on latitude, we chose 40 points at random from the interval,  $1.30M < r < 1.60M$ .

Figure 13 is a false color contour plot of a cross-section of the Boyer-Lindquist density in code units. Of the total of 40 field lines that were plotted, 15 were jet field lines. In this time slice there were 1 type I field line, 11 type II field lines, 3 type III field lines and 0 type IV field lines. So if the time slice,  $t = 9840 M$ , could be construed as a predominantly a type I event to the north, the time slice,  $t = 9920 M$ , could be considered a type II event to the south. The field lines emerging to the south from the inner edge of the accretion flow explain the direction of the white arrows (azimuthally averaged poloidal Poynting vector) in the top right hand frame of figure 3. These field lines are the source of the powerful narrow channel of radial Poynting flux that emerges from the ergosphere in the top right frame of figure 3. Notice that the field lines that form the southern jet displace large volumes of gas as they exit the inner accretion flow. Low density, magnetic regions (islands) are created just below the equatorial plane at the base of the jet. We note that the significant number of type III field lines in the northern jet could not have been anticipated from the azimuthally averaged plot in the top right hand frame of figure 3. Careful inspection of figure 13 shows that two of the type III field lines lie almost on top of one another in the northern jet.

### 4.4. The time-slice $t = 10000 M$

The magnetic field configuration at  $t = 10000 M$ , near the black hole, is the most complicated of the three time slices. There is a strong jet to the north that is very similar to the southern jet that was seen at  $t = 9920M$  and there is a modest southern jet. There was evidence of this southern jet in the azimuthal average of  $S^r$  in the bottom frame of figure 3 in the form of two disconnected patches of red and yellow. However, it was unclear if this represented two pieces of a continuous jet and there was not enough visual evidence to determine the 3-D magnetic field configuration that was responsible for these regions of enhanced  $S^r$ . Figure 14 is an alternative visualization to the wide angle view of a jet that

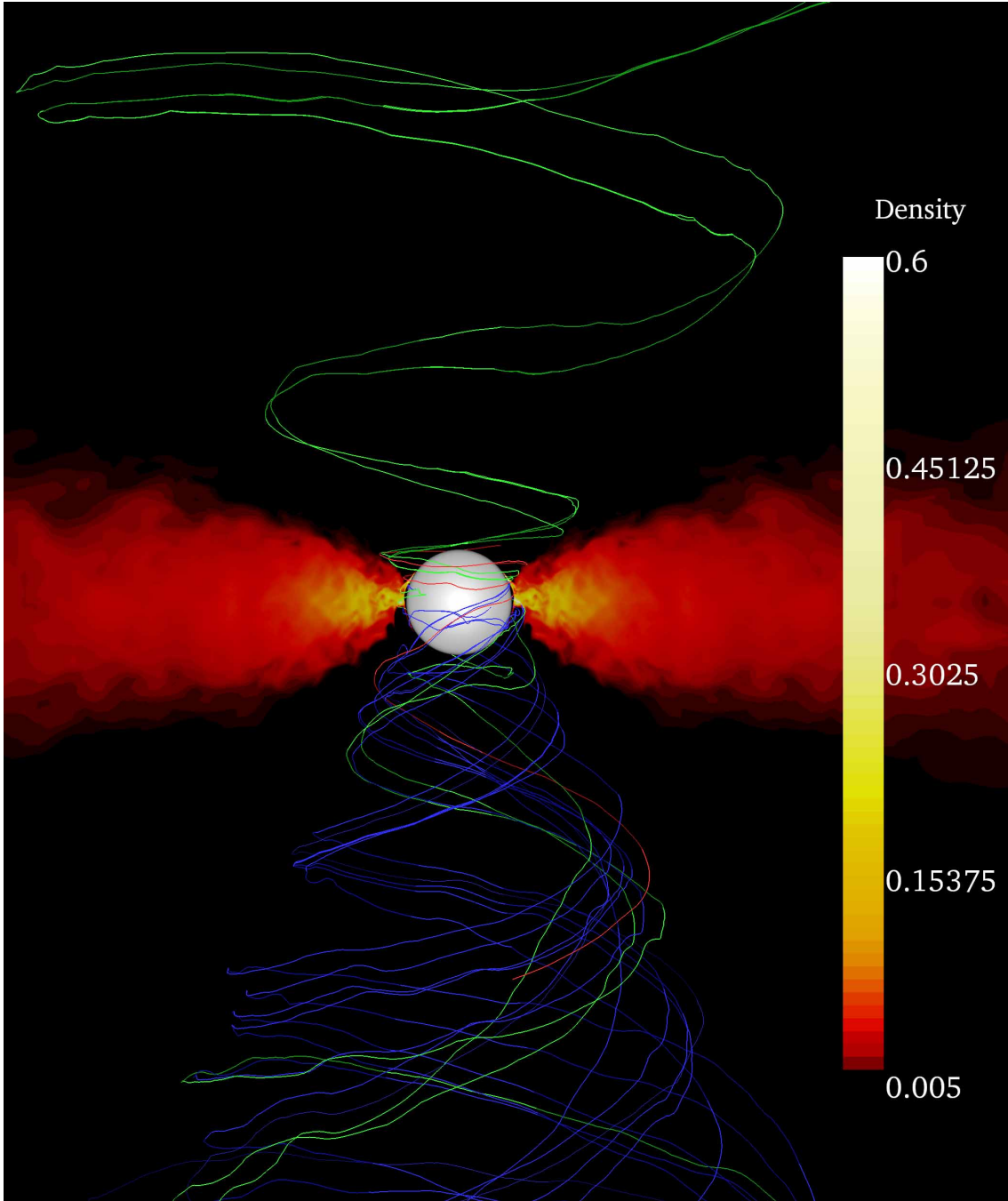


Fig. 13.— The wide angle view of the ergospheric disk jet at  $t = 9920 M$ . This is a false color plot of a cross-section of the Boyer-Lindquist evaluated density. The color bar on the right hand side is in code units. The magnetic field lines are color coded as described in section 4.3

was presented in figures 4 and 13. Instead of a false color contour plot of a cross-section of the density, we plot two 3-D density contours overlaid on top of each other, similar to figure 10. Such a representation of the density is conducive to a 3-D visualization of the jet/accretion flow interaction (since the gas is semi-transparent for all lines of sight) that is optimally displayed in the form of an animation of the Paraview camera rotating through different viewing angles to the black hole. Figure 14 is the last frame of the on-line animation, movie 4. The density contours are chosen at 0.05 and 0.1, with opacities of 40% and 35%, respectively. The line of sight from the Paraview camera to the black hole is in the equatorial plane. The camera swings around the black hole spin axis in the counter-clockwise direction.

Figure 14 and movie 4 show bipolar jets propagating away from the inner accretion flow. The latitude of the starting points of integration was restricted to  $\pm 4^\circ$  of the equatorial plane. With this restriction on latitude, we chose 20 points at random from the interval,  $1.35M < r < 1.55M$ , and an additional 40 starting points for integration were chosen randomly from the interval,  $1.30M < r < 1.60M$ . This is the opposite of what was chosen at  $t = 9840 M$ . The motivation for this change is that the bottom frame of figure 3, indicated that there was likely some interaction of the field lines comprising the southern jet with the accreting gas near  $r \lesssim 1.6M$ . A total of 27 out of the 60 field lines connect to the Poynting jets, 18 field lines go to the northern jet and 9 to the southern jet. Out of the 18 field lines that comprise the northern jet, 3 are type I, 12 are type II, 1 is type III and 2 are type IV. The 9 southern jet field lines are made up of 1 type III field line and 8 type IV field lines. The northern jet is basically a type I event and the southern jet is primarily a type IV event. Comparing the bottom frame of figure 3 with movie 4 and figure 14, one can understand the white arrows (the azimuthally averaged poloidal Poynting vector) at the base of the northern jet. A jet of predominantly type II field lines emerges vertically from the inner edge of the accretion flow. Once the coiled field lines reach a vertical elevation above the accretion flow they form a conical outflow that creates the strong channel of radial Poynting flux in the bottom frame of figure 3 (the bright red patch) that seems suspended outside the black hole and above the accretion disk. The southern jet (that is depicted by the white arrows that emerge latitudinally from the accretion flow in the bottom frame of figure 3) coincide with a new feature, the white type IV field lines that appear in figure 14.

#### 4.5. Overview of Findings

In this section we studied the distribution of vertical magnetic flux through the equatorial plane deep in the ergosphere of a rapidly rotating black hole in the simulation, KDJ.

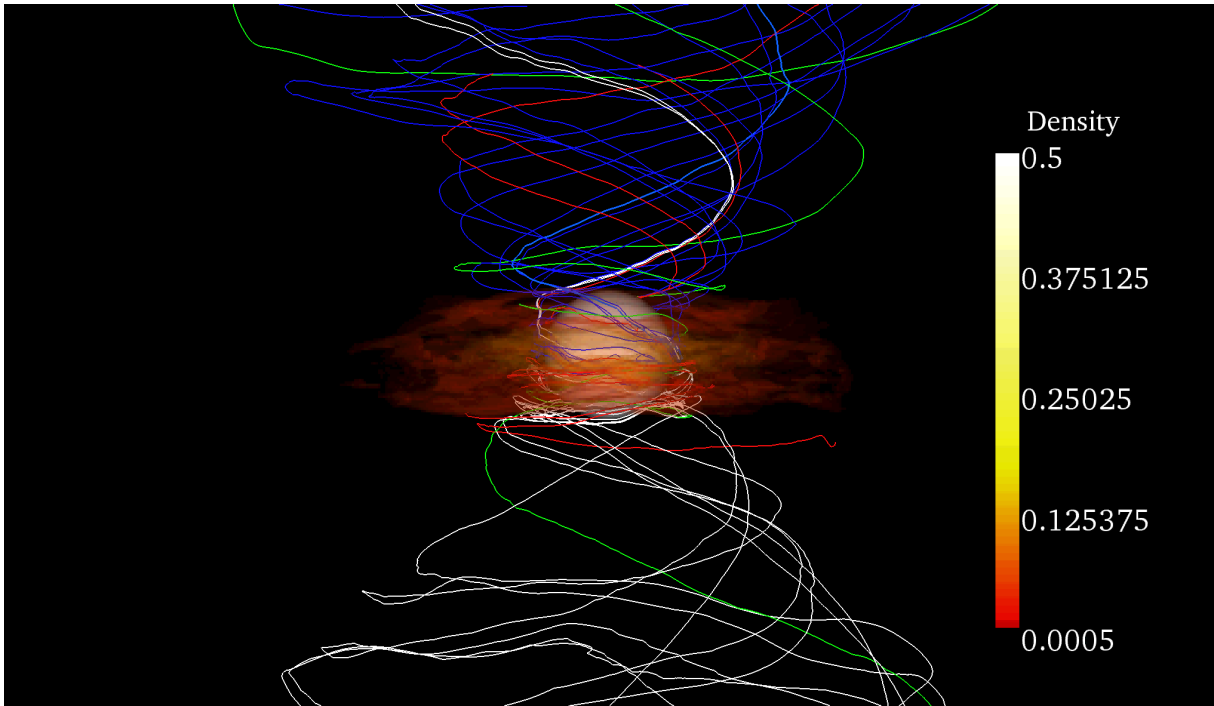


Fig. 14.— The wide angle view of the ergospheric disk jet at  $t = 10000 M$ . The image is the last frame of the on-line animation, movie 4. The density contours are chosen at 0.05 and 0.1, with opacities of 40% and 35%, respectively. The magnetic field lines are color coded as described in section 4.3. The interior of the inner calculation boundary is grayish-white.

We determined some potentially interesting results.

1. We found four distinct topological configurations for vertical flux through the equatorial plane in the inner ergosphere. The type I field lines (figure 6), type II field lines (figure 7), the type IV field lines (figure 9) are topologies for field lines that apparently were never envisioned based on theoretical work. The type III field line configuration (figure 8) was anticipated theoretically, but it is actually the rarest type of vertical field line that was found in the KDJ data.
2. All four forms of vertical flux through the inner accretion disk are associated with the high accretion rate analog of an ergospheric disk jet Punsly (2007a, 2008).
3. Regions of strong vertical field strength can temporarily suspend plasma outside of the event horizon. This magnetically arrested condition is illustrated in figure 12.
4. Bundles of strong magnetic field tends to create low density regions within the plasma (for type I field lines see animation 2, for type II field lines see figures 4, 5, 7 and 13).
5. Bundles of strong magnetic field tends to divert the accretion flow towards the opposite hemisphere (see figures 5, 12 and 13).
6. The vertical magnetic flux distribution is episodic and can not be described by the time stationary approximation (compare figures 4, 13 and 14).
7. The vertical magnetic flux and density distribution is inhomogeneous and can not be described within the context of 2-D.

We note that the discovery of vertical flux near the equatorial plane of the ergosphere in the simulation KDJ is in not accord with the results presented by one us earlier for a different simulation (Hirose et al 2004). Those results were based on 4 different numerical simulations with spin  $a/M = 0$ ,  $a/M = 0.5$ ,  $a/M = 0.9$  and  $a/M = 0.998$ . The simulations in Hirose et al (2004) were run before KDJ, which is part of a second generation of simulations in this same family. The only field line plots in Hirose et al (2004) that show field lines that don't penetrate the inner calculational boundary are for KDP,  $a/M = 0.9$ . It is concluded based on a classification scheme of Blandford (2002) that there are no class 7 field lines, lines that connect the plunge region to infinity. The type I - IV field lines that we find would be considered type 7 in that classification scheme. Both field line integration techniques are based on a fourth order Runge - Kutta scheme, so it is not the numerical method that accounts for the difference. Our field lines are not an artifact of the step size in the Runge - Kutta integration. As we pointed out in section 4.2.1, variations in the step size showed



only minor differences in the field line integrations, as long as the step size resolution was comparable to the grid resolution or finer. An occasional field line might integrate to a different topology with a variation in the integration step size, but the general situation is unchanged. For example, the following always hold as long a reasonable (not much coarser than the grid) step size is chosen, a strong patch of type I field lines always exists at the same azimuth at  $t = 9840 M$  as indicated in figure 5 and the strong magnetic wall of type II field lines at  $t = 9840 M$  always exists at the same azimuth as indicated in figure 12. Thus, we conclude that our results differ from Hirose et al (2004) because KDP does not have significant vertical flux in the inner accretion flow and KDJ does. We suspect that the only high spin simulation considered in Hirose et al (2004), KDE ( $a/M = 0.998$ ), might show some vertical flux in the ergosphere since there is a strong ergospheric disk jet in this simulation (Punsly 2008).

One might find the robustness of these topological identifications surprising in light of the fact that the disk is a turbulent medium. But, recall that the field lines in question tend to form magnetic islands in the accretion flow in regions where the density is typically only  $\sim 10\%$  of that in the center of the accretion flow (see sections 4.2.2 and 4.2.3). In these regions of equipartition and stronger poloidal fields, the MRI turbulence is suppressed (Stone and Pringle 2001; Balbus and Hawley 1991). In azimuthally averaged plots, the ergospheric disk jet is a well ordered region of strong poloidal field that penetrates the less dense regions of the accretion flow. The ergospheric jet field stands in obvious distinction to the adjacent, weaker random patches of turbulent poloidal field in the main body of the accretion flow. Therefore, the field line tangling discussed in Hirose et al (2004) is insignificant for the field lines described in this paper, except for the portion of the type I field lines that is restricted to hemisphere that is opposite of the hemisphere of the jet to which the field line is linked (see figure 6). More specifically, on the one hand, the extension of the type I field line toward the jet is not strongly tangled since it is in a region of strong magnetic field and low density (see the discussion at the end of section 4.2.3) and turbulence is minimized. On the other hand, as discussed in section 4.2.2, the type I field lines are anchored to the accretion flow in the opposite hemisphere and appear as a tangle of azimuthal twists with themselves and with other azimuthally twisting field lines. This anchoring end of the type I field lines have tangling characteristics similar to those found in figure 6 of Hirose et al (2004). However, this is unlikely to affect the jet launching physics to a significant degree since it lies below the source for the toroidal field in the jet (i.e., the point where the toroidal magnetic field changes sign on the type I field line within the disk - where the Poynting flux and toroidal field in the jet "originates"). The fate of the endlessly twisted portion of the type I field line does not affect its topological classification. The tangled end can go into the horizon, back out into the disk, or out into the corona; it is still the same topological classification. The

tangling of this end is irrelevant to the topological classification scheme. The only source of potential misidentification is if there are two type I field lines adjacent to each other in the accretion flow, one is coupled to a northern hemisphere jet and one is coupled to a southern hemisphere jet. Due to the finite grid size and turbulent mixing, one might misidentify this as a single type III field line. The fact that an individual time slice rarely shows type I field lines directed into two different hemispheres implies that this chance occurrence is rare. Furthermore, the fact that the type III field lines exit the disk in less than one orbit about the black hole means that there is minimal opportunity for tangling (see figure 8). Thus, we do not expect this misidentification to be the general case, but might occur occasionally if the field type III field line looked irregular (i.e., large gradients in the tangent direction) within the accretion flow.

In summary, the topological classification scheme is robust and the small scale turbulence on the dimension of the grid size does not affect the classification of type II and IV field lines. It could potentially lead to the misinterpretation of two oppositely directed type I field lines that are adjacent within the accretion flow as a single type III field line. If this rare coincidence happened, it is probably more of a pedantic distinction than a physical one.

With only three time snapshots, we might not have seen every possible topological form of vertical flux tube through the inner accretion flow. It is hard to imagine any other possible topology. However, that is one of the motivations for performing detailed numerical work. KDJ has already surprised us by finding type I, type II and type IV field lines that no one had ever envisioned. It would be interesting to rerun KDJ with the exact same code and initial state, but with much higher resolution to see if the higher resolution induces topological changes (do new types appear? do certain types disappear?). Also short time interval data dumps would be invaluable for seeing how the poloidal field evolves. Our findings are important not for fully categorizing the frequency of all the possible topological varieties in 3-D accretion flows, but for opening our eyes to the possible vertical field structures near accreting black holes within the context of the formation of strong Poynting jets.

## 5. Summary and Discussion

The dynamic nature of the inner regions of the accretion flow in KDJ and the simulation in Igumenshchev (2008) are quite different. Farther out in the main body of the accretion disk MRI driven turbulent viscosity transports angular momentum outward in both simulations. However, in Igumenshchev (2008), the turbulent region is restricted to a range of radii between the inner disk that is threaded by strong magnetic islands and  $r \approx 100M$  (an azimuthal cross section of the turbulent region looks similar to the turbulent region in

figure 1). A major distinction from KDJ is that within this turbulent region, the angular momentum is transported outward by both small scale magnetic torques (MRI turbulence) and large scale magnetic torques (associated with the net vertical flux through the equatorial plane) and in principle it is difficult to distinguish between the two. In the inner regions, it is large scale magnetic torques associated with the magnetic islands that is primarily responsible for extracting angular momentum from the plasma in Igumenshchev (2008). In KDJ, for most of the inflowing plasma near the black hole, turbulent viscosity torques the ingoing plasma except in localized magnetic islands where the ergospheric disk jet is launched. Near and within these magnetic islands, the dynamics of angular momentum redistribution is similar to Igumenshchev (2008). In spite of these differences, we found many results that are common to both extremes in black hole spin rate, as can be seen in the list of results, below.

1. All four types of vertical field lines around a rapidly rotating black hole support strong outward Poynting flux. There is also modest amounts of Poynting flux that is driven from the accretion flow along the vertical field lines in the Pseudo-Newtonian potential (see figure 3 for the Kerr case and Igumenshchev (2008) for the Pseudo-Newtonian potential).
2. In regions where vertical flux builds up in the inner accretion flow, the mass density goes down within that same region (see figure 2 for the Pseudo-Newtonian potential and figures 4, 5, 12 and 13 for the Kerr case).
3. The vertical flux build up (the formation of magnetic islands) is episodic and inhomogeneous. The distribution of vertical magnetic field in 3-D can not be described in the time stationary approximation (see figure 2 for the Pseudo-Newtonian potential and figures 4, 5, 11, 13 and 14 for the Kerr case).
4. The vertical flux distribution is inhomogeneous. The distribution of vertical magnetic field in 3-D can not be described in the 2-D approximation (see figure 2 for the Pseudo-Newtonian potential and figures 4, 5, 11, 13 and 14 for the Kerr case).
5. The flow can be temporarily arrested ( $dr/dt=0$ ) within and adjacent to the region of vertical flux build up (see figure 2 and Igumenshchev (2008) for the Pseudo-Newtonian potential and figure 12 for the Kerr case).
6. The flow is diverted by the magnetic pressure of the magnetic islands and tends to accrete in narrow channels or "spiral streams" that flow around the magnetic islands (see figures 2 for the Pseudo-Newtonian potential and figures 4, 5, 12, 13 and the

comment on the comparison of figures 4 and 5 with figure 8 in section 4.2.2 for the Kerr case).

The reason for the commonality within the list is clear. The existence of magnetic islands near a black hole is not a consequence of the dragging of inertial frames or the detailed history of how the magnetic flux reached the black hole to first order. MRI turbulence does not seem to produce significant Poynting jets in accretion flows as indicated in the test case simulations in Igumenshchev et al (2003); Beckwith et al (2008). It is the advection of a net poloidal field that creates the magnetic islands and the associated Poynting jet. In Igumenshchev (2008) this last statement is obvious by construction. In the poloidal loop simulations this is a bit more obscure. The field in the funnel is created by the leading edge of the accreted poloidal loops at the beginning of the simulation. The poloidal field orientation in the funnel at late times is always the same as the direction of the leading edge of the poloidal loops in the initial state torus (K. Beckwith and J. Hawley private communication 2008). The flux is trapped within the vortex and over time there are random fluctuations in the field distributions due to the MRI created poloidal fields that are considerably smaller, but the net radial field does not change sign. The poloidal field in the funnel is much stronger than the MRI generated poloidal field in the accretion flow. In KDJ, the strongest poloidal field is always at the base of the ergospheric disk jet and in the same direction as the funnel field. Thus, in KDJ it appears that it is the initial seed poloidal loops that were accreted that are ultimately the source of the poloidal flux in the magnetic islands in the inner accretion flow. This is consistent with results of the initial state parametric study performed in Beckwith et al (2008). If the leading edge of the initial state poloidal loops is destroyed by reconnection in the funnel or not there by construction, the funnel field and jet become insignificant or nonexistent (Beckwith et al 2008). The commonality between KDJ and the simulations in Igumenshchev (2008) listed above arise because both simulations have a net vertical flux accreted from distant regions into the immediate vicinity of the black hole.

The primary difference between the Pseudo-Newtonian case and the Kerr example is that the field is much more twisted due to strong frame dragging forces in the Kerr geometry. This has two primary effects. First, the azimuthal twists make the field lines look much more intricate and the resulting complexity of the magnetosphere is much greater. Another major difference is the amount of Poynting energy that is transported by the vertical field, there is at least an order of magnitude more in the Kerr case (about 1% - 2% of the accretion flow binding energy is transformed into Poynting flux in the Pseudo-Newtonian potential, Igumenshchev (2008), and about 25% of the accretion flow binding energy is transformed into Poynting flux in KDJ, Hawley and Krolik (2006); Punsly (2007a)).

There is another large difference that is not dependent on the black hole spin, but the assumptions of the simulations, there is no net vertical flux in KDJ and in the Pseudo-Newtonian simulations there is an infinite reservoir of vertical flux that is accreted. The end result is that there is much more vertical flux near the black hole in the Pseudo-Newtonian simulation. Presumably, accreting vertical flux from the outer boundary in the  $a/M = 0.99$  Kerr spacetime background would also result in an enhancement of vertical flux near the black hole relative to what was found in KDJ. We believe that if this were true, the vertical flux distribution and the accretion dynamics in the high spin case would closely resemble the simulations of Igumenshchev (2008). Presumably such an enhancement of vertical flux near the black hole would increase the extent of the ergospheric disk and the degree of magnetization. However, because of the nonlinear evolution of such a numerical system, a 3-D simulation of the  $a/M = 0.99$  black hole with vertical flux accretion from the outer boundary needs to be run to see if there is merit to these speculations. Figure 11.16 of Punsly (2008) is a plot based on the KDJ data that indicates that the jet power from the ergospheric disk is potentially 5 - 50 times more than can be derived from the Blandford-Znajek process that is associated with the event horizon magnetosphere. This ratio depends on spin rate and the degree to which the ergospheric disk is saturated with vertical flux. For example, with the degree of vertical flux saturation in KDJ with  $a/M=0.99$ , results in a ratio of ergospheric disk to Blandford-Znajek power of  $\gtrsim 5$ , for a completely saturated ergospheric disk with  $a/M = 0.995$ , the ratio is  $\approx 50$ . This result is also apparent from figure 3, where most of the power emerges in the narrow, red/yellow channels that are fed by the ergospheric disk. Without the ergospheric disk, one just has the blue background (the Blandford-Znajek power for the event horizon) in figure 3. An extremely efficient powerful jet seems to be a requirement of many powerful FR II radio sources (Punsly 2007c). In particular, vertical flux through the equatorial plane seems to be a viable candidate to support the more powerful FR II jets from low accretion rate (kinetically dominated) systems (see also Nemmen et al (2007) for similar conclusions).

In summary, in this paper we explored vertical magnetic flux in simulations of accretion flows near black holes. We categorized the magnetic field line topologies that were found and discussed conditions within the simulations that give rise to magnetic islands near black holes. One might wonder if there is any physical significance to the existence of vertical flux near a black hole or is it merely a pedantic exercise to distinguish between vertical flux and an axisymmetric event horizon magnetosphere. The motivation to differentiate the vertical flux from the horizon flux is two-fold. First of all, the strong interaction between vertical flux and the accretion flow has no counter-part in an event horizon magnetosphere located within the accretion vortex. The strong interaction was shown in this paper and in Igumenshchev (2008) to lead to episodic, inhomogeneous field configurations. It was posited

in Igumenshchev (2008) that this could be related to quasi-periodic oscillations in black hole binaries. Furthermore, the non-time stationary behavior could be related to high energy flares in AGN. Secondly, the existence of vertical flux increases the power of the Poynting jets from black hole accretion systems.

As a final comment, we mention the interesting 3-D numerical simulations performed by Fragile et al (2007). They have modeled accretion flows that are slightly inclined with respect to the equatorial plane. Surprisingly, it was found that merely tilting the accretion flow by  $15^\circ$  from the equatorial plane that the majority of the gas does not arrive at the equator of the event horizon, but at high latitudes near the poles. This creates low density cavities in the equatorial plane of the ergosphere. Now consider figures 5, 12 and 13 that seem to indicate that in KDJ, the existence of vertical flux that emerges from an accretion flow is correlated with the accretion flow being displaced toward the opposite hemisphere and the formation of low density cavities near the equatorial plane. Thus, it would be interesting to see if future higher resolution simulations of the tilted accretion disk naturally develop significant vertical flux emerging from the inner accretion flow within the ergosphere. However, we caution the reader that this code is quite different from that used in KDJ. Because of the lack of symmetry in the problem, it is difficult to get high numerical resolution in all the dynamically important regions. The simulations are likely to be too numerically diffusive for our goals and the results might not be a reliable indicator of magnetic flux evolution. A more reliable understanding of magnetic flux evolution in the tilted disk case might have to await future generations of simulations.

### A. Appendix. Field Line Integration Method

We describe our method of plotting field lines in 3-D using Paraview 3.3.0. This is nontrivial since the Boyer-Lindquist coordinate system is tantamount to a differentiable mapping of the spherical Minkowski coordinates,  $(t, r, \theta, \phi)$  defined in  $R^4$  into the curved spacetime outside of inner calculational boundary of the computational grid. In order to display three dimensional geometries (such as the magnetic field fibration of a subset of the spacetime outside the inner calculational boundary) embedded in the curved Kerr spacetime requires imaging in the our flat space 3-D world,  $R^3$ . Thus, this mapping into  $R^3$  for visualization purposes is not an isometric mapping from the Kerr spacetime. In particular, the 3-D visualization software Paraview only reads the magnetic field data in flat space Cartesian coordinates,

$$\mathbf{B} = (B^x(x, y, z), B^y(x, y, z), B^z(x, y, z)) . \tag{A1}$$

Paraview uses a Runge-Kutta scheme to integrate the following ordinary differential equation to draw field lines  $(x(s), y(s), z(s))$ :

$$\frac{dx}{ds} = \frac{B^x}{\|B\|} \quad (\text{A2})$$

$$\frac{dy}{ds} = \frac{B^y}{\|B\|} \quad (\text{A3})$$

$$\frac{dz}{ds} = \frac{B^z}{\|B\|}, \quad (\text{A4})$$

where

$$\|B\|^2 \equiv (B^x)^2 + (B^y)^2 + (B^z)^2 \quad (\text{A5})$$

$$ds^2 \equiv dx^2 + dy^2 + dz^2. \quad (\text{A6})$$

On the other hand, the Boyer-Lindquist coordinate system is analogous to a spherical coordinate system in which the magnetic field components are given in terms of the Faraday tensor in Punsly (2008) as

$$\mathbf{B} = (B^r(r, \theta, \phi), B^\theta(r, \theta, \phi), B^\phi(r, \theta, \phi)) = (F_{\theta\phi}(r, \theta, \phi), F_{\phi r}(r, \theta, \phi), F_{r\theta}(r, \theta, \phi)). \quad (\text{A7})$$

In Boyer-Lindquist coordinates, the magnetic field lines are defined by the following system of equations

$$\frac{dr}{ds} = \frac{B^r}{\|B\|} \quad (\text{A8})$$

$$\frac{d\theta}{ds} = \frac{B^\theta}{\|B\|} \quad (\text{A9})$$

$$\frac{d\phi}{ds} = \frac{B^\phi}{\|B\|}, \quad (\text{A10})$$

where

$$\|B\|^2 \equiv g_{rr}B^{r2} + g_{\theta\theta}B^{\theta2} + g_{\phi\phi}B^{\phi2} \quad (\text{A11})$$

$$ds^2 \equiv g_{rr}dr^2 + g_{\theta\theta}d\theta^2 + g_{\phi\phi}d\phi^2. \quad (\text{A12})$$

One can realize the Boyer-Lindquist magnetic field line definition in equations (A.8) - (A.12) in the context of flat space Cartesian coordinates (suitable for Paraview 3.3.0) by differentiating the transformation from Cartesian to spherical coordinates,

$$x \equiv r \sin \theta \cos \phi \quad (\text{A13})$$

$$y \equiv r \sin \theta \sin \phi \quad (\text{A14})$$

$$z \equiv r \cos \theta, \quad (\text{A15})$$

on both sides by the affine parameter "ds". Then the quantities,  $dr/ds$ ,  $d\theta/ds$  and  $d\phi/ds$ , that appear after differentiation by "ds" can be replaced with the right hand side of (A.8) - (A.10) to get

$$\frac{dx}{ds} = \frac{(B^r) \sin \theta \cos \phi + (rB^\theta) \cos \theta \cos \phi - (r \sin \theta B^\phi) \sin \phi}{\|B\|} \quad (\text{A16})$$

$$\frac{dy}{ds} = \frac{(B^r) \sin \theta \sin \phi + (rB^\theta) \cos \theta \sin \phi + (r \sin \theta B^\phi) \cos \phi}{\|B\|} \quad (\text{A17})$$

$$\frac{dz}{ds} = \frac{(B^r) \cos \theta - (rB^\theta) \sin \theta}{\|B\|}. \quad (\text{A18})$$

We integrate equations (A.16) - (A.18) with Paraview 3.3.0 for the field line data from the simulation KDJ.

We would like to thank Jean-Pierre DeVilliers for sharing his deep understanding of the numerical code and these simulations. We were also very fortunate that Julian Krolik and John Hawley were willing to share their data in the best spirit of science. This study was partially supported by the U.S. Department of Energy (DOE) Office of Inertial Confinement Fusion under Cooperative Agreement No. DE-FC52-08NA28302, the University of Rochester, the New York State Energy Research and Development Authority.

## REFERENCES

- Archontis, V., Hood, A., 2008, ApJ **647** 113
- Balbus, S. A., & Hawley, J. F. 1991, ApJ **376** 214
- Beckwith, K., Hawley, J., Krolik, J. 2008, ApJ **678** 1180
- Bisnovatyi-Kogan, G. S. and Ruzmaikin, A. A. 1974, Ap & SS **28** 45
- Bisnovatyi-Kogan, G. S. and Ruzmaikin, A. A. 1976, Ap & SS **42** 401
- Blandford, R. D. 1976, MNRAS **176** 465
- Blandford, R. D. 2002, in **Lighthouses of the Universe: The Most Luminous Celestial Objects and Their Use for Cosmology**, ed. M. Gilfanov, R. Sunyaev, & E. Churazov (New York: Springer), 381
- Blandford, R. D. and Payne, D., 1982, MNRAS **199** 883



- Blandford, R. and Znajek, R. 1977, MNRAS. **179**, 433
- Cabral, B., & Leedom, L. 1993, Computer Graphics: Proceedings: Annual Conference Series 1993: SIGGRAPH 93 (New York: Association for Computing Machinery), 263
- Colella, P., & Woodward, P.R. 1984, J. Comp. Phys., 54, 174
- De Villiers, J., Hawley, 2003, ApJ **589**, 458
- De Villiers, J-P., Hawley, J., Krolik, 2003, ApJ **599** 1238
- De Villiers, J-P., Hawley, J., Krolik, J., Hirose, S. 2005, ApJ **620** 878
- Dorch, S., Archontis, V., Nordlund, A., 1999, A & A **352** L79
- Fragile, P.C., Blaes, O.M., Anninos, P., Salmonson, J.D. 2007, ApJ **668** 417
- Gardiner, T.A., & Stone, J.M. 2005, J. Comp. Phys., 205, 509
- Ghosh, P., & Abramowicz, M. A. 1997, MNRAS **292**, 887
- Hawley, J., Krolik, K. 2006, ApJ **641** 103
- Hirose, S., Krolik, K., De Villiers, J., Hawley, J. 2004, ApJ **606**, 1083
- Igumenshchev, I. V. 2008, ApJ **677** 317
- Igumenshchev, I. V., Narayan, R. and Abramowicz, M. A. 2003, ApJ **592** 1042
- Kantrowicz, A.R. and Petschek, H.E. 1966, In: *Plasma Physics in Theory and Application*. ed. by W.B. Kunkel (McGraw-Hill, New York) p. 148
- Kato, Y., Mineshige, S. and Shibata, K. 2004, ApJ **605** 307
- Komissarov, S. 2004, MNRAS **350** 1431
- Komissarov, S., McKinney, J. 2007, MNRAS **377** 49
- Krolik, K., Hawley, J., Hirose, S. 2005, ApJ **622**, 1008
- Kulkarni, A., Romanova, M. M. 2008, MNRAS **386** 673
- Landau, L. D., & Lifshitz, E. M. 1987, *Electrodynamics of Continuous Media*. Pergamon Press, Oxford
- Lovelace, R. V. E. 1976, Nature **262** 649

- Lubow, S. H., Papaloizou, J. C. B and Pringle, J. E. 1994, MNRAS **267** 235
- McKinney, J. and Gammie, C. 2004, ApJ **611** 977
- McKinney, J. 2004, ApJL**630** 5
- Meier, D. L. 2004, ApJ **605** 340
- Narayan, R., Igumenshchev, I. V. and Abramowicz, M. A. 2003, PASJ **55** L69
- Nemmen, R., Bower, R., Babul, A., Storchi-Bergmann, T. 2007, MNRAS **377** 1652
- Paczynski, B., & Wiita, P.J. 1980, A&A, 88, 23
- Punsly, B., Coroniti, F.V. 1990, ApJ **354** 583
- Punsly, B. 1996, ApJ **467** 105
- Punsly, B. 2008, *Black Hole Gravitohydromagnetics*, second edition (Springer-Verlag, New York)
- Punsly, B. 2007, ApJL **661**, 21
- Punsly, B. 2007, MNRAS Letters **381**,79
- Punsly, B. 2007, MNRAS **374** 10
- Reynolds, C., Garofalo, D. and Begelman, M. 2006, ApJ **651** 1023
- Romanova, M. M., Kulkarni, A. and Lovelace, R. V. E. 2008, ApJ **673** 171
- Rothstein, D. and Lovelace, R. V. E. 2008, ApJ **677** 1221
- Semenov, V., Dyadechkin, S. and Punsly, B. 2004, Science **305**978
- Shibata, K., Tajima, T., Matsumoto, R. 1990, ApJ **350** 295
- Spruit, H.C. and Uzdensky, D.A. 2005, ApJ **629** 960
- Stone, J. M. and Pringle, J. 2001, MNRAS, **322**, 461
- Thorne, K., Price, R. and Macdonald, D. 1986, *Black Holes: The Membrane Paradigm* (Yale University Press, New Haven)
- Ustyugova, G. V., Lovelace, R. V. E., Romanova, M. M., Li, H and Colgate, S. 2000, ApJL **541** 21

van Ballegoijen, A. A. 1989, in ASSL Vol. 156 **Accretion Disks and Magnetic Fields in Astrophysics**, ed. G. Belvedere (Dordrecht: Kluwer Academic Publishers), 99

Warren, H. et al, 2008, ApL **686**, 131